

# Quantized Hall drift in a frequency-encoded photonic Chern insulator

A. Chénier,<sup>1</sup> B. d'Aligny,<sup>2,3</sup> F. Pellerin,<sup>1</sup> P.-É. Blanchard,<sup>1</sup> T. Ozawa,<sup>4</sup> I. Carusotto,<sup>2</sup> and P. St-Jean<sup>1,5</sup>

<sup>1</sup>*Département de Physique, Université de Montréal, C.P. 6128, Succursale Centre-Ville, Montréal, Québec, Canada H3C 3J7*

<sup>2</sup>*Pitaevskii BEC Center, INO-CNR and Dipartimento di Fisica, Università di Trento, via Sommarive 14, I-38123 Trento, Italy*

<sup>3</sup>*Ecole Polytechnique, Institut Polytechnique de Paris, 91128, Palaiseau, France*

<sup>4</sup>*Advanced Institute for Materials Research (WPI-AIMR), Tohoku University, Sendai 980-8577, Japan*

<sup>5</sup>*Institut Courtois, Université de Montréal, Montréal, Québec, Canada*

The prospect of developing more efficient classical or quantum photonic devices through the suppression of backscattering is a major driving force for the field of topological photonics. However, genuine protection against backscattering in photonics requires implementing architectures with broken time-reversal which is technically challenging. Here, we make use of a frequency-encoded synthetic dimension scheme in an optical fibre loop platform to experimentally realise a photonic Chern insulator inspired from the Haldane model where time-reversal is explicitly broken through temporal modulation. The bands' topology is assessed by reconstructing the Bloch states' geometry across the Brillouin zone. We further highlight its consequences by measuring a driven-dissipative analogue of the quantized transverse Hall conductivity. Our results thus open the door to harnessing topologically protected unidirectional transport of light in frequency-multiplexed photonic systems.

Chern insulators are a topological phase of matter with broken time-reversal symmetry ( $\mathcal{T}$ ) [1, 2]. A prominent example is provided by the quantum Hall effect, where the defining feature of topology is the emergence of backscattering-immune transport channels along the edges giving rise to quantized plateaux in the transverse conductivity [3, 4]. These robust channels hold significant value for applications requiring extensive resilience against environmental noise, e.g. in metrology [5], quantum computing [6] and information processing [7].

Extending this quantum Hall physics to photonics could allow engineering devices where the suppression of backscattering leads to enhanced performances and smaller footprints [8, 9]. This endeavour currently faces a two-fold challenge. On the one-hand, breaking  $\mathcal{T}$  through magneto-optical effects is technically challenging at optical or near-infrared frequencies due to the vanishing Verdet constant of most materials in this band; thus a lasing action is often necessary to probe  $\mathcal{T}$ -broken topological systems [10, 11]. On the other hand,  $\mathcal{T}$ -invariant photonic topological insulators are easier to realise but are inherently prone to backscattering [12]. Indeed, Kramer's degeneracy theorem which precludes the hybridization of counter-propagating electrons in  $\mathcal{T}$ -invariant topological matter doesn't apply to bosonic fields [13].

In this work, we introduce and demonstrate a novel approach to realising photonic Chern insulators that do not rely on strong external magnetic fields. We focus on the Haldane model [14] where  $\mathcal{T}$  is broken by adding complex next-nearest-neighbour couplings to a honeycomb lattice. This model was first realised with cold atoms in optical lattices [15, 16] and, more recently, has also been reported in the solid-state in temporally modulated monolayers [17] and in twisted Moiré bilayers [18, 19]. The key challenge in implementing Haldane phases, especially in the photonic context [20–22], lies in the strict requirements for inter-site connectivity within the lattice.

To overcome this challenge, we capitalize on the concept of synthetic dimensions which roots in the use of some internal degrees of freedom of a particle to mimic spatial coordinates [23, 24]. Here, we make use of the cavity modes of light confined in an optical fibre loop to encode a honeycomb lattice in frequency space. Independent tuning of the inter-site hopping amplitude and phase is achieved via suitable electro-optical modulation of the loop's refractive index [25–27]. This allows implementing the Haldane model across its topological phase diagram while maintaining clearly resolved bandgaps. Taking profit of the driven-dissipative nature of our system, we realise a complete tomography of the Bloch modes to extract the Berry curvature over the Brillouin zone (BZ) and the resulting Chern number of each band. We further evidence the hallmark of quantum Hall physics: a quantized transverse drift of light in frequency space induced by a synthetic electric field.

*The Haldane model* – The Haldane model describes a honeycomb lattice with complex next-nearest neighbour (NNN) couplings. In the tight-banding approximation, it is described by a 2-band Hamiltonian:

$$\mathcal{H}(\mathbf{k}) = \mathbf{h}(\mathbf{k}) \cdot \vec{\sigma}, \quad (1)$$

with  $\mathbf{k}$  spanning the BZ and  $\vec{\sigma} = (\sigma_x, \sigma_y, \sigma_z)$  the Pauli matrices. Eigenstates can be expressed as spinors:

$$|\psi_{\mathbf{k}}^{(\pm)}\rangle = \cos(\theta_{\mathbf{k}}^{(\pm)}/2) |a\rangle + \sin(\theta_{\mathbf{k}}^{(\pm)}/2) e^{i\phi_{\mathbf{k}}^{(\pm)}} |b\rangle. \quad (2)$$

with  $\{|a\rangle, |b\rangle\}$  the sub-lattice basis,  $\theta_{\mathbf{k}}^{(\pm)}$  and  $\phi_{\mathbf{k}}^{(\pm)}$  the polar and azimuthal angles on the Bloch sphere, and superscripts  $\pm$  identifying the lower/upper band.

In a honeycomb lattice with only nearest-neighbour (NN) couplings, as for graphene, inversion ( $\mathcal{I}$ ) and  $\mathcal{T}$  impose  $h_z(\mathbf{k}) = 0$ . This leads to the emergence of band touching points in reciprocal space, labelled  $K$

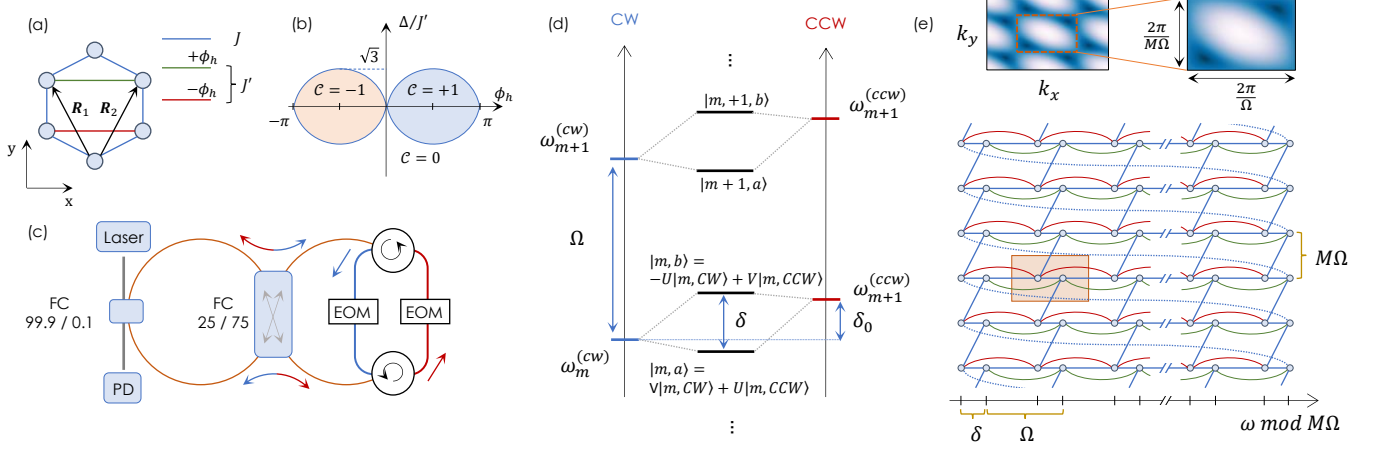


**FIG. 1. Implementation of the Haldane model in the synthetic frequency dimension.** (a) Schematic representation of our simplified Haldane model with NN couplings (blue lines) and a single pair of NNN couplings (red and green lines) of opposite phase ( $\pm\phi_h$ ) for each sub-lattice. (b) Topological phase diagram, as a function of  $\phi_h$  and  $\Delta/J'$ , exhibiting three distinct phases with Chern number  $\mathcal{C} = 0, \pm 1$ . (c) Schematic representation of the experimental setup depicting a single loop whose CCW (red arrows) and CW (blue arrows) circulating modes are coupled with a 25/75 fiber coupler (FC). On the right side, a pair of optical circulators allows modulating CW and CCW modes individually. The loop is probed with a photodiode (PD), using a transmission line coupled to the main loop with a 99.9% transmission FC. (d) Optical mode structure for two pairs of supermodes  $|i, a\rangle, |i, b\rangle$  with  $i = m, m + 1$ , formed from the coupling of CW and CCW modes split by a frequency  $\delta_0$ . (e) Representation of the brick-wall Haldane Hamiltonian with a folding period of  $M\Omega$  - each site represents a supermode of the fiber loop. A unit cell is depicted in orange. Blue lines indicate NN couplings with dotted lines indicating the twisted boundary conditions. NNN couplings are indicated with red and green lines for the  $|a\rangle$  and  $|b\rangle$  sublattices, respectively (for the sake of clarity, boundary conditions are not depicted for NNN couplings). The insets above depicts the associated reciprocal space (left) and a zoom on the first BZ.

and  $K'$  with  $K' = -K$ , around which the band dispersion is linear, similarly to Dirac fermions. These Dirac points carry remarkable topological signatures [28], evidenced by singularities in the Berry curvature  $\Omega_{\mathbf{k}}^{(\pm)} = \nabla \times \langle \psi_{\mathbf{k}}^{(\pm)} | i \partial_{\mathbf{k}} | \psi_{\mathbf{k}}^{(\pm)} \rangle$ .

The degeneracies at Dirac points can be lifted either by breaking  $\mathcal{I}$  or  $\mathcal{T}$ . In the former case, e.g. with inequivalent atoms in the unit cell as in hexagonal boron nitride (hBN), a constant mass term  $h_z(\mathbf{k}) = \Delta$  emerges. The bands are however topologically trivial with a vanishing Chern number  $\mathcal{C}^{(\pm)} = \frac{1}{2\pi} \int_{BZ} \Omega_{\mathbf{k}}^{(\pm)} \cdot d^2\mathbf{k}$ , as  $\mathcal{T}$  imposes  $\Omega_{\mathbf{k}}$  to be anti-symmetric in  $\mathbf{k}$ . In the latter case, the Berry curvature no longer necessarily integrates to zero, giving rise to topological bands with non-zero Chern number.

In the Haldane model,  $\mathcal{T}$  is broken by adding complex NNN couplings with amplitude  $J'$  and opposite phase  $\pm\phi_h$  for each sub-lattice. Differently from the original Haldane model, we only consider one pair of NNN coupling terms along  $\hat{x}$  (Fig. 1 (a)). This simplification does not qualitatively modify the topological phase diagram shown in Fig. 1 (b). The NNN coupling terms induce a  $\mathbf{k}$ -dependent mass term  $h_z(\mathbf{k}) = J' \sin(\mathbf{k} \cdot (\mathbf{R}_2 - \mathbf{R}_1)) \sin(\phi_h)$  which has the same amplitude but opposite sign at  $K$  and  $K'$ , leading to topologically non-trivial phases for  $|\Delta| < |\sqrt{3}J' \sin(\phi_h)|$ .

*Implementation in frequency space* - We realise the Haldane model using the frequency-periodic cavity modes of an optical fibre loop (Fig. 1 (c)) to form a

frequency-encoded honeycomb lattice in the brickwall geometry (Fig. 1 (e)). Unit cells are separated by the loop's free spectral range  $\Omega$  with the two sublattices formed from the hybridized supermodes, split by frequency  $\delta$ , that emerge from coupling the quasi-resonant clockwise (CW) and counter-clockwise (CCW) modes (Fig. 1 (d)).

Inter-site hoppings are tailored by independently modulating the CW and CCW fields with electro-optical phase modulators (EOM) driven at frequencies corresponding to the frequency spacing between pairs of supermodes [26, 29]. NN hoppings are realized by driving both EOMs with Fourier components at frequencies  $\delta$ ,  $\Omega - \delta$  and  $M\Omega + \delta$  (see Methods). The first two terms which describe coupling between adjacent frequency modes provide a first synthetic dimension. The second synthetic dimension is provided by the third, higher-frequency terms that couple modes separated by  $2M + 1$  lattice sites [30–32]. The resulting synthetic lattice shown in Fig. 1 (e) presents a reorganisation of the modes in frequency space with a  $M\Omega$  folding period. An effective brickwall lattice with twisted boundary conditions (dotted lines) emerges. The associated reciprocal space and a zoom-in on the first BZ are depicted in the top inset.

Finally, the NNN couplings of the Haldane model are implemented by including an additional component to the EOMs' driving field at frequency  $\Omega$  with opposite phase  $\pm\phi_h$  for each EOM. For this model specifically, we work in a regime where the bare CW and CCW modes are

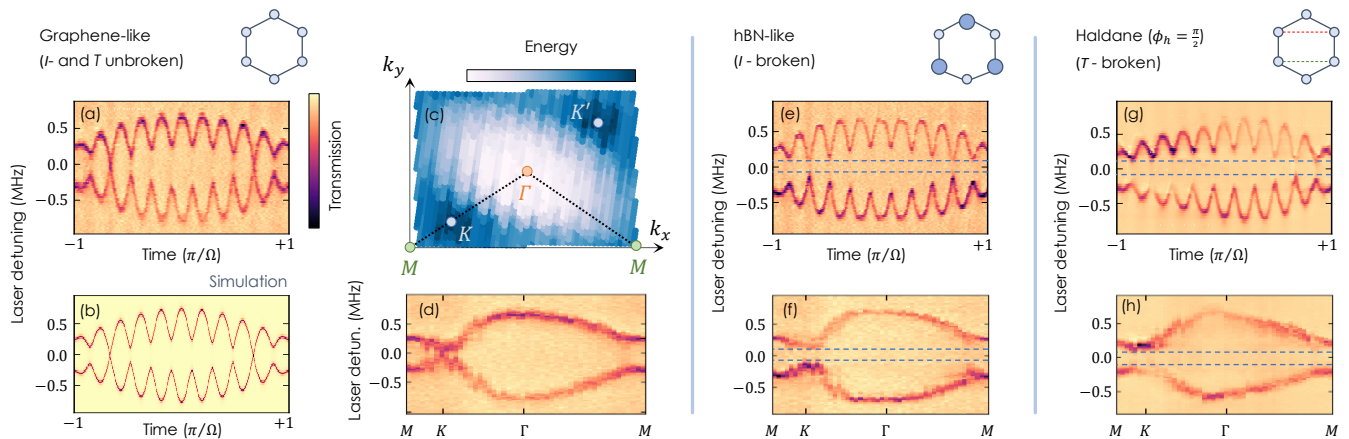


FIG. 2. **Band structure measurements for graphene-like, hBN-like and Haldane models.** (a),(e),(g) Band structure measurements for configurations emulating graphene (a), hexagonal boron nitride (e) and the Haldane model with  $\phi_h = \pi/2$  (g). The band dispersion is obtained by measuring the time-resolved transmission of the loop as a function of time and laser detuning. (b) The simulation of the graphene-like configuration agrees with the experimental results in (a). (c) Lower band dispersion as a function of  $(k_x, k_y)$ ; a fine coverage of the BZ is obtained by scanning the phase of one driving component. (d),(f),(h) Band dispersion along a trajectory through high-symmetry points  $M - K - \Gamma - M$  indicated in (c) for graphene-like (d), hBN-like (f) and the Haldane model (h). The latter two clearly show a bandgap, indicated by dashed horizontal lines.

not degenerate, so that each supermode has a dominant CW or CCW character, i.e.  $|U|^2 \gg |V|^2$  in Fig. 1 (d). This is critically important to obtain opposite phases for the NNN couplings of the  $|a, b\rangle$  sub-lattices, even though their splittings are equal  $\omega_m^{(a/b)} - \omega_{m+1}^{(a/b)} = \Omega$ .

*Band structure measurement* – While edge states are the natural observable for topological photonics systems in real-space [23, 33], synthetic frequency dimensions offer direct access to the bulk energy bands through time-resolved transmission measurement using a continuous-wave laser [26]. The principle underlying this measurement (see Methods and SM for details) is that the periodicity of the eigenmodes in frequency gives rise to time-periodic pulse trains with superposed long ( $T = \frac{2\pi}{\Omega}$ ) and short periods ( $T' = \frac{2\pi}{M\Omega}$ ) components. Each time bin  $t_i$  probes a single point  $\mathbf{k} = (t_i \bmod T, t_i \bmod T')$  within a BZ whose dimensions are inversely proportional to  $\Omega$  and  $M\Omega$ , respectively associated to the short- and long-range periodicity in frequency space. The transmitted signal exhibits intensity dips whenever the laser frequency is resonant with an energy band of the lattice.

This periodic signal is monitored on a photodiode while scanning the frequency of the laser. We plot in Fig. 2 the result averaged over 150 periods of length  $T$  with  $M = 10$ . For the case with only NN coupling terms with equal amplitude, which emulates the physics of graphene (Fig. 2 (a)), we observe two bands with one slow (period  $T$ ) and 10 fast (period  $T'$ ) oscillations, respectively associated to scans of the BZ along  $k_x$  and  $k_y$ . The band touching points associated to each Dirac point ( $K$  and  $K'$ ) are clearly visible, in very good agreement with theoretical simulations (Fig. 2 (b)).

This measurement is then reproduced by varying the phase of the Fourier component with frequency  $\Omega - \delta$

to follow slightly shifted trajectories in reciprocal space, thus producing a finer coverage of the BZ. In Fig. 2 (c), we plot the extracted energy of the lower band, showing very clearly the position of the Dirac points in accordance with the theory (inset in Fig. 1 (e)). Then, by selecting data at time bins along the high-symmetry  $M - K - \Gamma - M$  trajectory (dashed line), it is possible to generate the band structure in Fig. 2 (d).

Breaking  $\mathcal{I}$  in this lattice, thus emulating the physics of hBN, is realised by slightly shifting the EOM driving frequencies associated to NN coupling terms to  $\delta + \Delta$ ,  $\Omega - \delta - \Delta$  and  $M\Omega + \delta + \Delta$  with  $\Delta/2\pi = 200$  kHz. In the synthetic lattice, this detuning realises a staggered on-site potential giving rise to a mass term  $h_z(\mathbf{k}) = \Delta/2$ . Accordingly, we observe at each Dirac point the opening of a bandgap of  $E_g \sim 175$  kHz (Fig. 2 (e)-(f)), significantly larger than the optical linewidth ( $\gamma \sim 50$  kHz).

Breaking  $\mathcal{T}$  and realizing the Haldane Hamiltonian is achieved by adding the NNN component at frequency  $\Omega$ . Using a phase of  $\phi_h = \pi/2$ , setting  $\Delta = 0$  and working in a regime where  $|U|^2 \gg |V|^2$ , we again open a significant bandgap (Fig. 2 (g)-(h)). Interestingly, the intensity of each band changes as a function of  $\mathbf{k}$ , with the lower (upper) band reaching a vanishing intensity at  $K$  ( $K'$ ); this is a direct consequence of the mass term  $h_z(\mathbf{k})$  since the transmission measurement is performed along the CCW direction (see Methods).

*Extraction of the Berry curvature* – These transmission measurements further allow performing a full tomography of the eigenmodes across the BZ [34]. As the eigenmodes are linear combinations of CW and CCW modes but we measure the transmission along the CCW direction, the transmitted intensity is modulated in time at frequency  $\delta$  and, for each time bin in the BZ, the phase

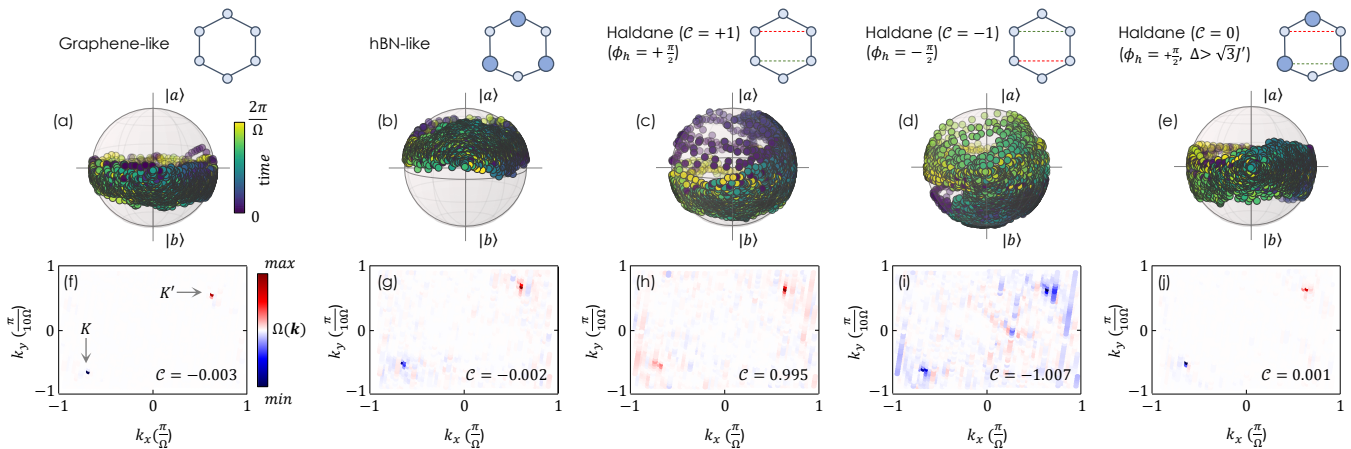


FIG. 3. **Extraction of the Berry curvature and Chern number.** (a)-(e) Tomographic measurement of the lower band's eigenstates  $|\psi_{\mathbf{k}}^{(+)}\rangle$  across the full BZ for the cases of graphene-like (a) and hBN-like (b) lattices, for topologically non-trivial Haldane model with  $\phi_h = +\pi/2$  (c) and  $\phi_h = -\pi/2$  (d), and topologically trivial Haldane model with  $\phi_h = +\pi/2$  and  $\Delta > \sqrt{3}J'$  (e). The north and south poles of the Bloch spheres correspond to the sub-lattice basis states  $|a\rangle$  and  $|b\rangle$  respectively. The colour code refers to the time bin of each  $k$ -point. (f)-(j) The Berry curvature, extracted using the Fukui method from the momentum-resolved eigenstates shown in Panels (a)-(e), exhibit clear peaks at the positions of the Dirac point  $K$  and  $K'$ . The value of the Chern number obtained by integrating the Berry curvature over the BZ is indicated in the corner of each panel.

of this beating exactly follows the azimuthal angle  $\phi_{\mathbf{k}}$  in Eq. 2. The polar angle  $\theta_{\mathbf{k}}$  indicating the eigenmodes' relative weight on the  $|a\rangle, |b\rangle$  sublattices is extracted from the intensity ratio between the two bands (see Methods).

The experimentally extracted values of  $\phi_{\mathbf{k}}, \theta_{\mathbf{k}}$  across the BZ can be plotted on a Bloch sphere (Fig. 3 (a)-(e)). For the case of graphene (a), the lower band's eigenstates  $|\psi_{\mathbf{k}}^{(+)}\rangle$  stays confined to the vicinity of the equator, as expected for  $h_z = 0$ . For hBN (b), the evolution is shifted to the northern hemisphere evidencing the effect of the constant mass term  $h_z = \Delta/2$ . For Haldane lattices with  $\phi_h = \pm\pi/2$  (c)-(d), the situation is drastically different: the opposite sign of the mass term  $h_z(\mathbf{k})$  between  $K$  and  $K'$  makes  $|\psi_{\mathbf{k}}^{(+)}\rangle$  explore the full Bloch sphere, indicating a non-trivial topology. The trajectory on the Bloch sphere is reversed when switching the sign of  $\phi_h$ . When we add a constant mass term  $\Delta > \sqrt{3}J'$  (e), the Bloch sphere is no longer entirely covered.

In order to quantitatively assess the bands' topology, we take profit of this tomography to extract the value of the Berry curvature across the entire BZ [35]. To do this, we use the technique developed in Ref. [36] for discretized BZs. The result is plotted below each Bloch sphere and the associated Chern number, extracted by summing  $\Omega_{\mathbf{k}}$  over the BZ, is indicated in the corner.

For graphene-like lattices, the Berry curvature is negligible over the entire BZ except in the close vicinity of  $K$  and  $K'$ . Sharply peaked Berry curvatures with opposite signs are observed close to  $K$  and  $K'$  points, leading to a vanishing Chern number; this is consistent with  $\mathcal{T}$ -symmetry of the graphene-like lattice. For hBN-like lattices, the situation is very similar as the Hamiltonian is still  $\mathcal{T}$ -symmetric but the peaks are broader in recip-

rocal space, as the Berry curvature spreads in  $\mathbf{k}$  when a bandgap opens. For the Haldane model, we clearly see that the two peaks now have the same sign, either positive for  $\mathcal{C} = +1$  or negative for  $\mathcal{C} = -1$ , as a direct consequence of the broken  $\mathcal{T}$ . The extracted Chern numbers are consistent with the expected values for topologically non-trivial phases. In the presence of a constant mass term  $\Delta > \sqrt{3}J'$ , the peaks recover opposite signs: this gives a vanishing Chern number as expected for a topologically trivial phase.

*Quantized Hall drift* – One of the most representative consequences of topology in quantum Hall [3, 4] and topological magnetic [37] systems is the emergence of plateaus in the transverse conductivity at values determined by the bands' Chern number. Here, we observe a driven-dissipative analogue of this effect with photons experiencing a quantized drift in frequency space.

We implement a synthetic electric field by adding a detuning  $\lambda$  to the Fourier component associated to the NN coupling term along  $\hat{y}$ . In the rotating frame, this induces a linearly varying detuning with respect to the loop's eigenmodes. Within the synthetic lattice picture (Fig. 4 (a)), this can be interpreted as a scalar potential  $V(y) = -\lambda y$  giving rise to a synthetic electric field  $\mathbf{E} = \lambda \hat{y}$  [38, 39]. The anomalous transverse displacement [28] induced by this synthetic electric field is measured according to the theoretical proposals in [40, 41] by injecting monochromatic light at a single lattice site and then detecting the centre-of-mass displacement of the steady-state distribution of light in frequency space. In our synthetic-dimension framework this is extracted by means of a heterodyne measurement (Fig. 4 (b)) where the signal radiating from the CCW and CW modes of the loop is mixed with the laser shifted by 200 MHz. A



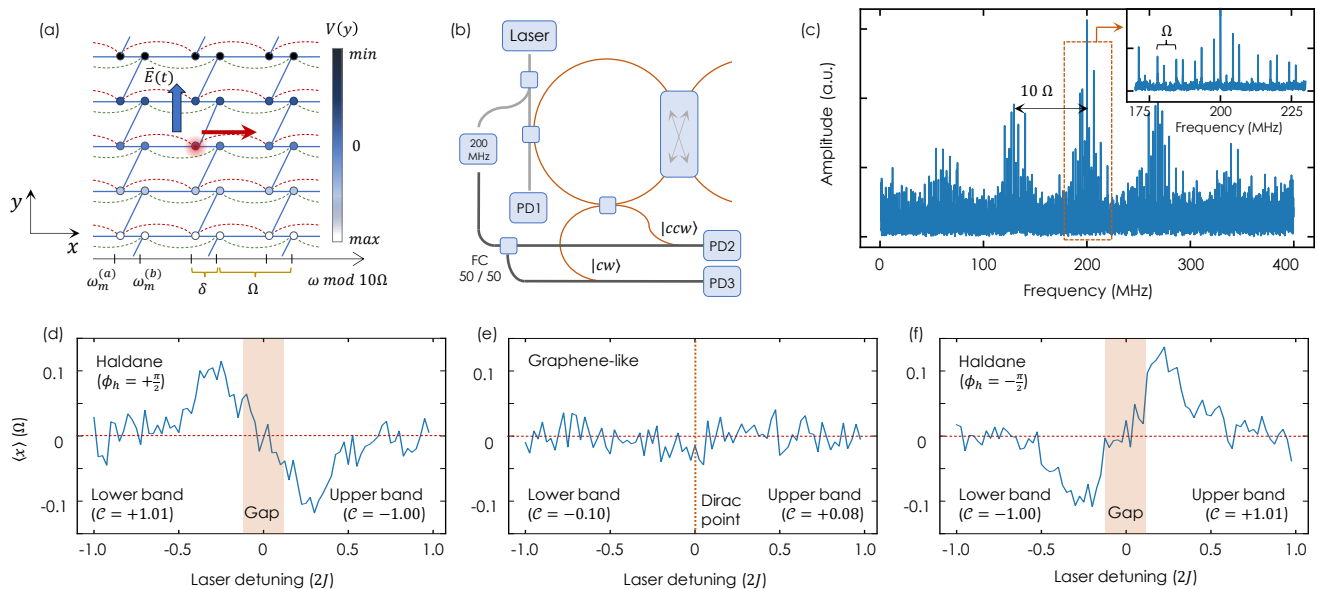


FIG. 4. **Photonic analogue of the transverse Hall conductivity in frequency space.** (a) Schematic representation of the experimental protocol for measuring the anomalous transverse displacement. The effective scalar potential induced by the detuning along  $\hat{y}$  is depicted by the blue colour gradient. The driven site is indicated by the red spot and the displacement by the red arrow. (b) Experimental setup for the heterodyne measurement. The local oscillator consists of the laser signal shifted by 200 MHz and split in two to beat with both the CCW and CW modes, respectively measured with photodiodes PD2 and PD3. (c) Example of a heterodyne spectrum exhibiting broad regions separated by  $10\Omega$  with a high density of narrowly-spaced peaks. The inset shows a zoom-in on the central region exhibiting pairs of peaks separated by  $\Omega$ . (d)-(f) Anomalous transverse displacement in units of the unit cell ( $\Omega$ ) as a function of the laser detuning in units of the bandwidth ( $2J$  with  $J$  the NN coupling strength) for two topologically distinct phases of the Haldane model (d) and (f), and a graphene-like lattice (e). For each band, we indicate the Chern number extracted by integrating the displacement over the laser detuning. The uncertainty on these values is  $\pm 0.10$  (see SM).

typical heterodyne spectrum obtained by adding the CW and CCW signals' Fourier transform is presented in Fig. 4 (c). Regions with closely spaced peaks are visible with a spacing of  $10\Omega$ , which correspond to distinct rows of the lattice; the inset gives a magnified view over the central region, where the spacing  $\Omega$  between the pairs of peaks corresponds to the lattice periodicity along  $\hat{x}$ . From this spectrum, we extract the wavepacket's center-of-mass position  $\langle x \rangle = \sum \omega I_\omega / \sum I_\omega$  (see details in the SM).

The expected anomalous displacement is limited to only a fraction of a unit cell, notably because of the relatively strong dissipation of our system. In order to accurately extract such a small quantity, we make use of frequency modulation to create a time-varying electric field  $\lambda(t) = \lambda_0 \sin(\Omega_\lambda t)$ . We then perform a quadrature demodulation of the heterodyne signal with  $\lambda(t)$  as the reference signal to isolate the Fourier component of  $\langle x \rangle$  that oscillates exactly at  $\Omega_\lambda$ .

The results are presented in Fig. 4 (d)-(f) as a function of the laser detuning. As the linewidth of each state in the bands is smaller than the overall width of the bands, the observed displacement probes the Berry curvature averaged over states overlapping with the laser and provides evidence of an anomalous Hall effect [35, 40, 42, 43]. For the Haldane model in (d) and (f), we observe significant

displacements when the laser is resonant with eigenmodes with a strong Berry curvature, i.e. at the top of the lower band and the bottom of the upper band. This displacement has opposite signs for the upper and lower bands as expected, and gets reversed when switching the topological phase. In contrast, no displacement is observed for the case of a graphene-like lattice.

While this anomalous displacement is of geometrical origin, a topologically quantized Chern number results from integrating the Berry curvature over the BZ. Here, it can be obtained by integrating the transverse displacement over the laser detuning. The result of such a procedure (see details in the SM) is indicated in the figure panels: within the experimental uncertainty, values compatible with 0 and  $\pm 1$  are obtained in the different cases, in accordance with the theory and with the geometry of the band states previously measured in Fig. 3. This quantization of the photonic transverse Hall drift is a clear signature of its robustness and universality, endowed by the bands' underlying topology.

*Conclusion* – Our work demonstrates a novel approach to realising photonic Chern insulators. In particular, the remarkable tunability and the intrinsic driven-dissipative nature of our platform has allowed us to perform a thorough characterisation of the bulk topological properties,

including the measurement of the band structures, of the Berry curvature, and of a photonic analogue of the quantized transverse Hall conductivity.

We envision that our platform will allow investigating high-dimensional topological systems beyond the three physical dimensions [25]. It also offers new avenues for further exploring the consequences of topologically non-trivial bands, including directional light-matter interaction phenomena in chiral environments [44–46], the emergence of one-way topological edge modes when translational symmetry in frequency space is broken [25, 47, 48]

and their peculiar coupling to bulk states [49]. On a longer run, extending our platform to the quantum non-linear regime opens a promising route to emulating topological quantum matter with fluids of light [50, 51].

From a technological perspective, our work opens new pathways, inspired by topological band theory, for robustly engineering the flow of light in frequency space. This advancement holds significant potential for a wide range of applications involving multi-frequency dynamics, including pulsed lasers [52, 53], frequency combs [54, 55], signal processing [56, 57], sensing [58, 59], time crystals [60, 61] and neural networks [62, 63].

- 
- [1] M. Z. Hasan and C. L. Kane, *Reviews of Modern Physics* **82**, 3045 (2010), publisher: American Physical Society.
- [2] X.-L. Qi and S.-C. Zhang, *Reviews of Modern Physics* **83**, 1057 (2011), publisher: American Physical Society.
- [3] D. J. Thouless, M. Kohmoto, M. P. Nightingale, and M. den Nijs, *Physical Review Letters* **49**, 405 (1982), publisher: American Physical Society.
- [4] R. E. Prange and S. M. Girvin, eds., *The Quantum Hall effect*, 2nd ed., Graduate texts in contemporary physics (Springer-Verlag, New York, 1990).
- [5] K. von Klitzing, *Physical Review Letters* **122**, 200001 (2019), publisher: American Physical Society.
- [6] C. Nayak, S. H. Simon, A. Stern, M. Freedman, and S. Das Sarma, *Reviews of Modern Physics* **80**, 1083 (2008), publisher: American Physical Society.
- [7] F. Zangeneh-Nejad, D. L. Sounas, A. Alù, and R. Fleury, *Nature Reviews Materials* **6**, 207 (2021), publisher: Nature Publishing Group.
- [8] T. Ozawa, H. M. Price, A. Amo, N. Goldman, M. Hafezi, L. Lu, M. C. Rechtsman, D. Schuster, J. Simon, O. Zilberberg, and I. Carusotto, *Reviews of Modern Physics* **91**, 015006 (2019), publisher: American Physical Society.
- [9] H. Price, Y. Chong, A. Khanikaev, H. Schomerus, L. J. Maczewsky, M. Kremer, M. Heinrich, A. Szameit, O. Zilberberg, Y. Yang, B. Zhang, A. Alù, R. Thomale, I. Carusotto, P. St-Jean, A. Amo, A. Dutt, L. Yuan, S. Fan, X. Yin, C. Peng, T. Ozawa, and A. Blanco-Redondo, *Journal of Physics: Photonics* **4**, 032501 (2022), publisher: IOP Publishing.
- [10] B. Bahari, A. Ndao, F. Vallini, A. El Amili, Y. Fainman, and B. Kanté, *Science* **358**, 636 (2017), publisher: American Association for the Advancement of Science.
- [11] S. Klembt, T. H. Harder, O. A. Egorov, K. Winkler, R. Ge, M. A. Bandres, M. Emmerling, L. Worschech, T. C. H. Liew, M. Segev, C. Schneider, and S. Höfling, *Nature* **562**, 552 (2018), publisher: Nature Publishing Group.
- [12] C. A. Rosiek, G. Arregui, A. Vladimirova, M. Albrechtsen, B. Vosoughi Lahijani, R. E. Christiansen, and S. Stobbe, *Nature Photonics* **17**, 386 (2023), publisher: Nature Publishing Group.
- [13] L. Lu, J. D. Joannopoulos, and M. Soljačić, *Nature Physics* **12**, 626 (2016), publisher: Nature Publishing Group.
- [14] F. D. M. Haldane, *Physical Review Letters* **61**, 2015 (1988), publisher: American Physical Society.
- [15] G. Jotzu, M. Messer, R. Desbuquois, M. Lebrat, T. Uehlinger, D. Greif, and T. Esslinger, *Nature* **515**, 237 (2014), publisher: Nature Publishing Group.
- [16] N. Fläschner, D. Vogel, M. Tarnowski, B. S. Rem, D.-S. Lühmann, M. Heyl, J. C. Budich, L. Mathey, K. Senstock, and C. Weitenberg, *Nature Physics* **14**, 265 (2018), publisher: Nature Publishing Group.
- [17] S. Mitra, A. Jiménez-Galán, M. Aulich, M. Neuhaus, R. E. F. Silva, V. Pervak, M. F. Kling, and S. Biswas, *Nature* **628**, 752 (2024), publisher: Nature Publishing Group.
- [18] W. Zhao, K. Kang, Y. Zhang, P. Knüppel, Z. Tao, L. Li, C. L. Tschirhart, E. Redekop, K. Watanabe, T. Taniguchi, A. F. Young, J. Shan, and K. F. Mak, *Nature Physics* **20**, 275 (2024), publisher: Nature Publishing Group.
- [19] J. Cai, E. Anderson, C. Wang, X. Zhang, X. Liu, W. Holtzmann, Y. Zhang, F. Fan, T. Taniguchi, K. Watanabe, Y. Ran, T. Cao, L. Fu, D. Xiao, W. Yao, and X. Xu, *Nature* **622**, 63 (2023), publisher: Nature Publishing Group.
- [20] L. He, Z. Addison, J. Jin, E. J. Mele, S. G. Johnson, and B. Zhen, *Nature Communications* **10**, 4194 (2019), publisher: Nature Publishing Group.
- [21] Y. G. N. Liu, P. S. Jung, M. Parto, D. N. Christodoulides, and M. Khajavikhan, *Nature Physics* **17**, 704 (2021), publisher: Nature Publishing Group.
- [22] S. K. Sridhar, S. Ghosh, D. Srinivasan, A. R. Miller, and A. Dutt, *Nature Physics* **20**, 843 (2024), publisher: Nature Publishing Group.
- [23] T. Ozawa and H. M. Price, *Nature Reviews Physics* **1**, 349 (2019), publisher: Nature Publishing Group.
- [24] L. Yuan, Q. Lin, M. Xiao, and S. Fan, *Optica* **5**, 1396 (2018), publisher: Optica Publishing Group.
- [25] T. Ozawa, H. M. Price, N. Goldman, O. Zilberberg, and I. Carusotto, *Physical Review A* **93**, 043827 (2016), publisher: American Physical Society.
- [26] A. Dutt, M. Minkov, Q. Lin, L. Yuan, D. A. B. Miller, and S. Fan, *Nature Communications* **10**, 3122 (2019), publisher: Nature Publishing Group.
- [27] S. Sriram, S. K. Sridhar, and A. Dutt, “Quantized topological phases beyond square lattices in Floquet synthetic dimensions,” (2024), arXiv:2411.02475.
- [28] D. Xiao, M.-C. Chang, and Q. Niu, *Reviews of Modern Physics* **82**, 1959 (2010), publisher: American Physical Society.

- [29] A. Dutt, Q. Lin, L. Yuan, M. Minkov, M. Xiao, and S. Fan, *Science* **367**, 59 (2020), publisher: American Association for the Advancement of Science.
- [30] L. Yuan, M. Xiao, Q. Lin, and S. Fan, *Physical Review B* **97**, 104105 (2018), publisher: American Physical Society.
- [31] A. Senanian, L. G. Wright, P. F. Wade, H. K. Doyle, and P. L. McMahon, *Nature Physics* **19**, 1333 (2023), publisher: Nature Publishing Group.
- [32] D. Cheng, E. Lustig, K. Wang, and S. Fan, *Light: Science & Applications* **12**, 158 (2023), publisher: Nature Publishing Group.
- [33] S. Mittal, V. V. Orre, D. Leykam, Y. Chong, and M. Hafezi, *Physical Review Letters* **123**, 043201 (2019), publisher: American Physical Society.
- [34] F. Pellerin, R. Houvenaghel, W. Coish, I. Carusotto, and P. St-Jean, *Physical Review Letters* **132**, 183802 (2024), publisher: American Physical Society.
- [35] A. Gianfrate, O. Bleu, L. Dominici, V. Ardizzone, M. De Giorgi, D. Ballarini, G. Lerario, K. W. West, L. N. Pfeiffer, D. D. Solnyshkov, D. Sanvitto, and G. Malpuech, *Nature* **578**, 381 (2020), publisher: Nature Publishing Group.
- [36] T. Fukui, Y. Hatsugai, and H. Suzuki, *Journal of the Physical Society of Japan* **74**, 1674 (2005), publisher: The Physical Society of Japan.
- [37] C.-Z. Chang, C.-X. Liu, and A. H. MacDonald, *Reviews of Modern Physics* **95**, 011002 (2023), publisher: American Physical Society.
- [38] G. Li, Y. Zheng, A. Dutt, D. Yu, Q. Shan, S. Liu, L. Yuan, S. Fan, and X. Chen, *Science Advances* **7**, eabe4335 (2021), publisher: American Association for the Advancement of Science.
- [39] C. Oliver, A. Smith, T. Easton, G. Salerno, V. Guarrera, N. Goldman, G. Barontini, and H. M. Price, *Physical Review Research* **5**, 033001 (2023), publisher: American Physical Society.
- [40] T. Ozawa and I. Carusotto, *Physical Review Letters* **112**, 133902 (2014), publisher: American Physical Society.
- [41] T. Ozawa, *Physical Review B* **97**, 041108 (2018), publisher: American Physical Society.
- [42] M. Wimmer, H. M. Price, I. Carusotto, and U. Peschel, *Nature Physics* **13**, 545 (2017), publisher: Nature Publishing Group.
- [43] I. T. Rosen, S. Muschinske, C. N. Barrett, A. Chatterjee, M. Hays, M. A. DeMarco, A. H. Karamlou, D. A. Rower, R. Das, D. K. Kim, B. M. Niedzielski, M. Schuldt, K. Serniak, M. E. Schwartz, J. L. Yoder, J. A. Grover, and W. D. Oliver, *Nature Physics* , 1 (2024), publisher: Nature Publishing Group.
- [44] M. Bello, G. Platero, J. I. Cirac, and A. González-Tudela, *Science Advances* **5**, eaaw0297 (2019), publisher: American Association for the Advancement of Science.
- [45] J. C. Owens, M. G. Panetta, B. Saxberg, G. Roberts, S. Chakram, R. Ma, A. Vrajitoarea, J. Simon, and D. I. Schuster, *Nature Physics* **18**, 1048 (2022), publisher: Nature Publishing Group.
- [46] D. De Bernardis, F. S. Piccioli, P. Rabl, and I. Carusotto, *PRX Quantum* **4**, 030306 (2023), publisher: American Physical Society.
- [47] A. Dutt, L. Yuan, K. Y. Yang, K. Wang, S. Buddhiraju, J. Vučković, and S. Fan, *Nature Communications* **13**, 3377 (2022), publisher: Nature Publishing Group.
- [48] D. G. Reid, C. Oliver, P. Regan, A. Smith, T. Easton, G. Salerno, G. Barontini, N. Goldman, and H. M. Price, “Topological Chiral Edge States in a Synthetic Dimension of Atomic Trap States,” (2024), arXiv:2410.10501.
- [49] Z. Zhu, M. Gächter, A.-S. Walter, K. Viebahn, and T. Esslinger, *Science* **384**, 317 (2024), publisher: American Association for the Advancement of Science.
- [50] C.-K. Chiu, J. C. Teo, A. P. Schnyder, and S. Ryu, *Reviews of Modern Physics* **88**, 035005 (2016), publisher: American Physical Society.
- [51] I. Carusotto, A. A. Houck, A. J. Kollár, P. Roushan, D. I. Schuster, and J. Simon, *Nature Physics* **16**, 268 (2020), publisher: Nature Publishing Group.
- [52] C. R. Leefmans, M. Parto, J. Williams, G. H. Y. Li, A. Dutt, F. Nori, and A. Marandi, *Nature Physics* **20**, 852 (2024), publisher: Nature Publishing Group.
- [53] Z. Yang, E. Lustig, G. Harari, Y. Plotnik, Y. Lumer, M. A. Bandres, and M. Segev, *Physical Review X* **10**, 011059 (2020), publisher: American Physical Society.
- [54] S. Mittal, G. Moille, K. Srinivasan, Y. K. Chembo, and M. Hafezi, *Nature Physics* **17**, 1169 (2021), publisher: Nature Publishing Group.
- [55] Y. Hu, C. Reimer, A. Shams-Ansari, M. Zhang, and M. Loncar, *Optica* **7**, 1189 (2020), publisher: Optica Publishing Group.
- [56] M. Zhang, B. Buscaino, C. Wang, A. Shams-Ansari, C. Reimer, R. Zhu, J. M. Kahn, and M. Lončar, *Nature* **568**, 373 (2019), publisher: Nature Publishing Group.
- [57] S. Buddhiraju, A. Dutt, M. Minkov, I. A. D. Williamson, and S. Fan, *Nature Communications* **12**, 2401 (2021), publisher: Nature Publishing Group.
- [58] J. C. Budich and E. J. Bergholtz, *Physical Review Letters* **125**, 180403 (2020), publisher: American Physical Society.
- [59] A. McDonald and A. A. Clerk, *Nature Communications* **11**, 5382 (2020), publisher: Nature Publishing Group.
- [60] E. Lustig, Y. Sharabi, and M. Segev, *Optica* **5**, 1390 (2018), publisher: Optica Publishing Group.
- [61] N. I. Zheludev, *Nature Photonics* **18**, 1123 (2024), publisher: Nature Publishing Group.
- [62] L. Fan, K. Wang, H. Wang, A. Dutt, and S. Fan, *Science Advances* **9**, eadi4956 (2023), publisher: American Association for the Advancement of Science.
- [63] C. C. Wanjura and F. Marquardt, *Nature Physics* **20**, 1434 (2024), publisher: Nature Publishing Group.
- [64] L. Yuan and S. Fan, *Physical Review Letters* **114**, 243901 (2015), publisher: American Physical Society.

## Methods.

*Optical fibre loop setup.* In order to work in a single polarization state, the entire platform is formed from polarization maintaining fibred components. The polarization is oriented along the fast axis of the lithium niobate crystal in the electro-optical phase modulators. The CW and CCW circulating modes of the fiber-loop are coupled with a 25:75 fibre coupler (FC).

The resulting eigenmodes are the hybridized supermodes:

$$\begin{aligned} |m, a\rangle &= U |m, \text{CCW}\rangle + V |m, \text{CW}\rangle \\ |m, b\rangle &= V |m, \text{CCW}\rangle - U |m, \text{CW}\rangle \end{aligned} \quad (3)$$

split by  $\delta/2\pi = 2\sqrt{g^2 + (\delta_0/2)^2}/2\pi$ , with  $g \sim 1.1$  MHz the strength of the effective coupling induced by the FC and  $\delta_0 = \omega_m^{(cw)} - \omega_m^{(ccw)}$  the splitting between the CW and CCW uncoupled modes. The precise value of this splitting changes depending on the measurement (see SM). On the other hand, the lattice periodicity  $\omega_m^{(a/b)} - \omega_{m+1}^{(a/b)}$  is constant and is given by the free spectral range:  $\Omega/2\pi \sim 6.6$  MHz.

*EOM modulation.* The NN couplings are induced by driving the EOMs with the field:

$$\begin{aligned} V_{nn}^{(cw/ccw)}(t) &= \pm \frac{1}{2} \left[ V_{nn}^{(1)} e^{-i\delta t} + V_{nn}^{(2)} e^{-i(\Omega-\delta)t} \right. \\ &\quad \left. + V_{nn}^{(3)} e^{-i(M\Omega+\delta)t} \right] + \text{c.c.} \end{aligned} \quad (4)$$

with + and - corresponding to the modulation of the CW and CCW modes respectively. The NNN coupling terms are induced by adding the following Fourier components to the EOMs' driving field:

$$V_{nnn}^{(cw/ccw)}(t) = \frac{1}{2} V_{nnn}^{(0)} e^{-i(\Omega t \pm \phi_n)} + \text{c.c.} \quad (5)$$

where the sign of the phase differs for CW (+) and CCW (-) modes. Implementation of the graphene-like Hamiltonian is achieved using  $V_{nn}^{(1)} = V_{nn}^{(2)} = V_{nn}^{(3)}$  and  $V_{nnn}^{(0)} = 0$ . The hBN-like Hamiltonian is realized by introducing slight detunings of the NN couplings:

$$\begin{aligned} \delta &\rightarrow \delta + \Delta \\ \Omega - \delta &\rightarrow \Omega - \delta - \Delta \\ M\Omega + \delta &\rightarrow M\Omega + \delta + \Delta. \end{aligned} \quad (6)$$

with  $\Delta/2\pi = 200$  kHz.

*Transmission measurements.* The measurement is performed using a narrow-linewidth ( $\Delta\omega < 5$  kHz) continuous-wave laser and a high-bandwidth photodiode (DC-250 MHz). Upon modulating the loop, we measure the band structures by measuring the transmitted signal intensity – along the CCW direction – which follows the

relation (see SM):

$$\begin{aligned} \frac{I^{(+)}(t)}{|F|^2} &\sim 1 - 2\kappa \text{Re} \left\{ \frac{f_{\mathbf{k}}^{(+)}(t)}{\frac{\gamma}{2} - i(\Delta\omega_L - \epsilon_{\mathbf{k}}^{(+)})} \right\} \Bigg|_{(k_x, k_y)} \\ \frac{I^{(-)}(t)}{|F|^2} &\sim 1 - 2\kappa \text{Re} \left\{ \frac{f_{\mathbf{k}}^{(-)}(t)}{\frac{\gamma}{2} - i(\Delta\omega_L - \epsilon_{\mathbf{k}}^{(-)})} \right\} \Bigg|_{(k_x, k_y)} \end{aligned} \quad (7)$$

where  $F$  and  $\Delta\omega_L$  are the driving field amplitude and detuning with respect to the loop's closest eigenmodes,  $\gamma$  and  $\kappa$  are the loop's total decay rate and input-output-coupling ratio, and each time  $t$  corresponds to a  $\mathbf{k}$ -point in the BZ via  $\mathbf{k} = (k_x = t \bmod T, k_y = t \bmod T')$ . The denominators in Eq. 7 therefore leads to Lorentzian intensity dips whenever the laser is resonant with the lower/upper band dispersions  $\epsilon_k^{(\pm)}$  at crystal momentum  $k_x, k_y$ . The numerators  $f_k^{(\pm)}$  are given by:

$$\begin{aligned} f_{\mathbf{k}}^{(+)} &= U^2 \cos^2\left(\frac{\theta_{\mathbf{k}}}{2}\right) + UV \sin\left(\frac{\theta_{\mathbf{k}}}{2}\right) \cos\left(\frac{\theta_{\mathbf{k}}}{2}\right) e^{-i\delta t} e^{i\phi_{\mathbf{k}}} \\ f_{\mathbf{k}}^{(-)} &= U^2 \sin^2\left(\frac{\theta_{\mathbf{k}}}{2}\right) - UV \cos\left(\frac{\theta_{\mathbf{k}}}{2}\right) \sin\left(\frac{\theta_{\mathbf{k}}}{2}\right) e^{-i\delta t} e^{i\phi_{\mathbf{k}}} \end{aligned} \quad (8)$$

where we have used the shorthand  $\theta_{\mathbf{k}} = \theta_{\mathbf{k}}^{(+)}$  and  $\phi_{\mathbf{k}} = \phi_{\mathbf{k}}^{(+)}$  and we have taken into account that  $\theta_{\mathbf{k}}^{(-)} = \pi - \theta_{\mathbf{k}}^{(+)}$  and  $\phi_{\mathbf{k}}^{(-)} = \pi + \phi_{\mathbf{k}}^{(+)}$ . These quantities carry information on the polar and azimuthal angles  $\theta_{\mathbf{k}}^{(\pm)}, \phi_{\mathbf{k}}^{(\pm)}$  of the Bloch eigenstates.

The band structures reported in Fig. 2 are experimentally obtained by averaging over the measurement of 150 BZs, thus averaging out the modulation terms oscillating at frequency  $\delta$  in the numerators  $f_{\mathbf{k}}^{(\pm)}$ . The normalized difference of the time-averaged intensities  $[\bar{f}_{\mathbf{k}}^{(+)} - \bar{f}_{\mathbf{k}}^{(-)}]/[\bar{f}_{\mathbf{k}}^{(+)} + \bar{f}_{\mathbf{k}}^{(-)}]$  of the lower and upper bands is equal to  $\cos(\theta_{\mathbf{k}})$ . This allows extracting the polar angle of the eigenmodes on the Bloch sphere reported in Fig. 3. The azimuthal angle is obtained by extracting the phase of the temporal modulation at frequency  $\delta$  of the transmitted intensity (given by the time dependence of the numerators in Eqs. 8). This phase  $\phi_k$  is obtained by taking the Fourier transform of the transmitted signal measured at specific time bins  $t \bmod T$ , and extracting the phase of the Fourier component at frequency  $\delta$ .

*Heterodyne measurement.* In order to remove the large signal coming from the transmitted laser, the heterodyne measurements are performed by collecting light radiating from a distinct output port than the input port used for injecting light. We measure independently the signal from the CW and CCW ports using two high-bandwidth photodiodes (DC-600 MHz). This provides complete information on the intensity of both sublattices as they are linear combinations of CW and CCW modes. The local



oscillator consists of the laser field shifted by 200 MHz.

*Synthetic electric field.* The synthetic electric field in frequency space is generated by modulating the frequency of the  $V_{nm}^{(3)}$  component :

$$M\Omega + \delta \rightarrow M\Omega + \delta + \lambda(t) \quad (9)$$

with  $\lambda(t) = \lambda_0 \sin(\Omega_\lambda t)$  where  $\lambda_0/2\pi = 10$  kHz and  $\Omega_\lambda/2\pi = 100$  kHz. This modulated electric field allows extracting with a high signal-to-noise ratio the wavepacket displacement by demodulating the time evolution of the centre of mass with  $\lambda(t)$  as a demodulation reference. This allows isolating the Fourier component of  $\langle x \rangle$  at the electric field oscillating frequency.

*Experimental measurement of the Chern number.* The Chern number is experimentally extracted from the transverse displacement of the intensity distribution in response to the synthetic electric field. For a fixed laser frequency  $\omega_L$ , the transverse displacement  $\langle \Delta x \rangle_{\omega_L}$  is proportional to the averaged Berry curvature along the iso- $\omega_L$  lines. The Chern number  $\mathcal{C}$  of a band is then recovered by integrating over the energy range of the band with a suitable weight according to

$$\mathcal{C} = -\frac{\gamma^2}{4\pi^2 \lambda_0} \int_{\text{band}} d\omega_L \langle \Delta x \rangle_{\omega_L} \int \frac{d^2 \mathbf{k}}{(\epsilon_{\mathbf{k}} - \omega_L)^2 + (\gamma/2)^2}. \quad (10)$$

**Acknowledgements.** We acknowledge insightful discussions with W. A. Coish. PSJ acknowledges financial support from Québec's Fonds de Recherche-Nature et Technologies (FRQNT), Canada's Natural Sciences and Engineering Research Council (NSERC) and Québec's Ministère de l'Économie, de l'Innovation et de l'Énergie. IC acknowledges financial support from the Provincia Autonoma di Trento, from the Q@TN Initiative, and from the National Quantum Science and Technology Institute through the PNRR MUR Project under Grant PE0000023-NQSTI, co-funded by the European Union - NextGeneration EU. TO acknowledges financial support from JSPS KAKENHI Grant Number JP24K00548, JST PRESTO Grant No. JPMJPR2353, and JST CREST Grant Number JPMJCR19T1.

**I. SUPPLEMENTARY MATERIAL: QUANTIZED HALL DRIFT  
IN A FREQUENCY-ENCODED PHOTONIC CHERN INSULATOR**

**CONTENTS**

References	6
I. Supplementary Material: Quantized Hall drift in a frequency-encoded photonic Chern insulator	10
II. Experimental setup	11
A. Optical Setup	11
B. Electrical Setup	12
III. Experimental protocol	12
A. Calibration procedure	12
1. Calibration of the free spectral range $\Omega$	12
2. Calibration of the sub-lattice spacing $\delta$	13
B. Band Structure Measurements	15
C. Berry Curvature measurement	16
1. Extraction of $\phi_{\mathbf{k}}$	17
2. Extraction of $\theta_k$	17
3. Mapping on the Bloch sphere	18
4. Extraction of the Berry curvature	18
D. Anomalous Transverse Displacement	19
IV. Theoretical framework	20
A. Derivation of the Haldane Hamiltonian	20
1. Derivation of the NN Hamiltonian	21
2. Derivation of the NNN Hamiltonian	22
B. Derivation of the time-resolved transmission measured by the photodiode	23
C. Anomalous transverse displacement and Chern number extraction	26

## II. EXPERIMENTAL SETUP

### A. Optical Setup

A schematic of the optical setup is presented in Fig. 5 (a). We use a Grade 3 Rio Orion laser emitting with a central wavelength of 1542.27nm and with a linewidth of 3.1 kHz. A tunable optical attenuator is used to limit the optical power in the cavity and mitigate non-linear effects. The output of the laser is split by a fibre coupler with 1 % sent toward the main loop and the rest continuing to a 200 MHz frequency shifter to be used as a local oscillator (LO) in the heterodyne measurement. A 99.9:0.1 fibre coupler is used as the entry port to the main loop. The transmitted intensity is measured with a 250 MHz bandwidth InGaAs photodiode connected to a digitizer. This signal is used for measuring band structures and performing wave-function tomography.

All optical components in the setup are polarization maintaining to ensure perfect alignment with the optical axes of the electro-optical modulators; a polariser is used to further ensure proper polarization filtering. A semiconductor optical amplifier (SOA) is used to amplify the optical signal inside the cavity in order to compensate for the losses caused by the different components inside the loop and ensure a high quality factor ( $Q \sim 4 \times 10^9$ ). The resulting finesse of the cavity is  $\mathcal{F} \sim 120$ . A 100 GHz bandwidth filter is used to suppress the amplification of undesired modes.

Inside the loop, a 75:25 fiber coupler is used to hybridize the two directions of propagation inside the cavity. As described in the main text, this fibre coupler hybridizes counter-propagating modes; the resulting supermodes form the lattice sites in the synthetic frequency dimension. In order to efficiently implement nearest-neighbour (NN) and next-nearest-neighbour coupling terms (NNN) – the latter with opposite phases for different sub-lattices –, we separate the CW and CCW propagating modes with a pair of circulators. This allows time-modulating independently CW and CCW modes with iXBlue lithium niobate electro-optical phase modulators. Each branch also includes an isolator to ensure unidirectional propagation in-between the circulators.

A second 99.9:0.1 fibre coupler is used as an output port to realise the heterodyne measurement. The use of a second port allows probing simultaneously the CW and CCW modes. The LO for the heterodyne measurement is provided by the laser shifted by 200 MHz and amplified with an erbium doped fibre amplifier (EDFA). This LO is then split in half with a 50:50 fibre coupler and then mixed (using 99:1 fibre couplers) with the signal radiating from the CW and CCW modes output ports. Two InGaAs photodiodes with a bandwidth of 600 MHz are used for collecting these mixed signals.

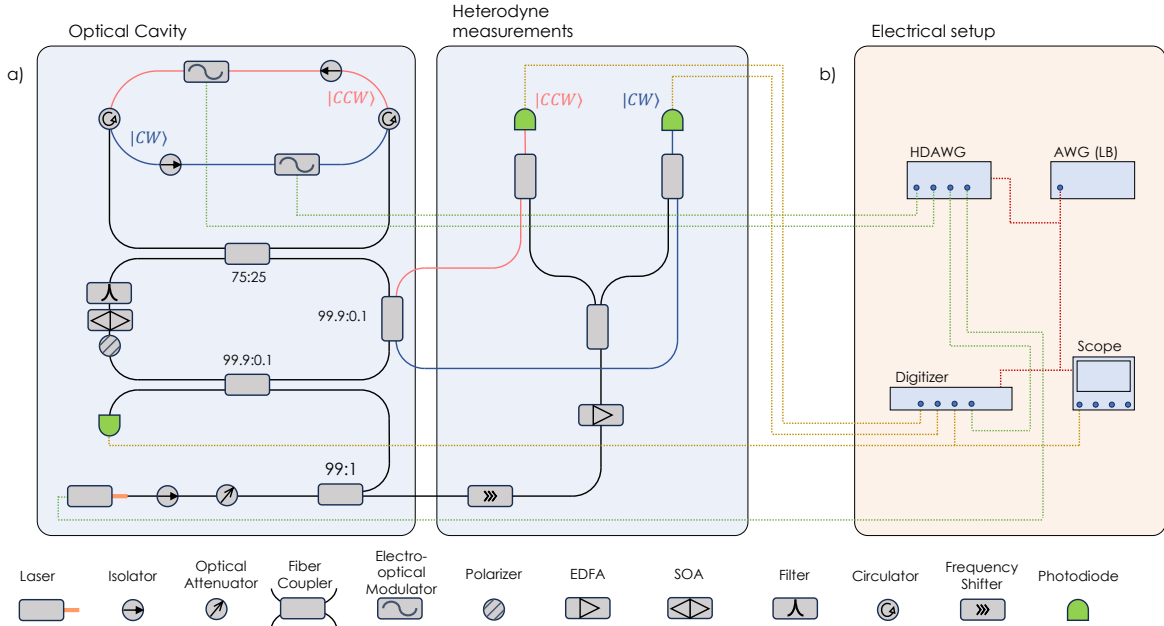


FIG. 5. Schematic representation of the experimental setup

## B. Electrical Setup

A schematic of the full electrical setup can be seen in figure 5 (b). The electrical signal from the photodiode measuring the transmission signal is split in two toward a 2 GHz-bandwidth Rigol oscilloscope and a Tektronix 6 Series Low Profile digitizer (with a bandwidth of 2.5 GHz and a sampling rate of  $25 \text{ GSs}^{-1}$ ). This allows probing the signal over two different time windows, each with high temporal resolution; the window measured on the oscilloscope is used as a calibration probe and the window measured on the digitizer is used to register the actual experiment data (see calibration section).

The electrical signals driving the EOMs and tuning the laser frequency are provided by a Zurich Instruments High Definition Arbitrary Waveform Generator (HDAWG). A low bandwidth arbitrary waveform generators, generating a low frequency square wave, is also used to trigger all our electrical instruments simultaneously.

## III. EXPERIMENTAL PROTOCOL

### A. Calibration procedure

The calibration consists in determining the values of  $\Omega$  (the FSR) and  $\delta/2\pi = 2\sqrt{g^2 + (\delta_0/2)^2}/2\pi$  (the splitting between the two sub-lattices) with  $\delta_0$  the CW-CCW frequency splitting. Accurate determination of these two frequencies is critical for driving the EOMs with the appropriate signal in order to not induce spurious on-site energies and/or electric fields. Hereafter, we detail the procedure for calibrating each frequency.

#### 1. Calibration of the free spectral range $\Omega$

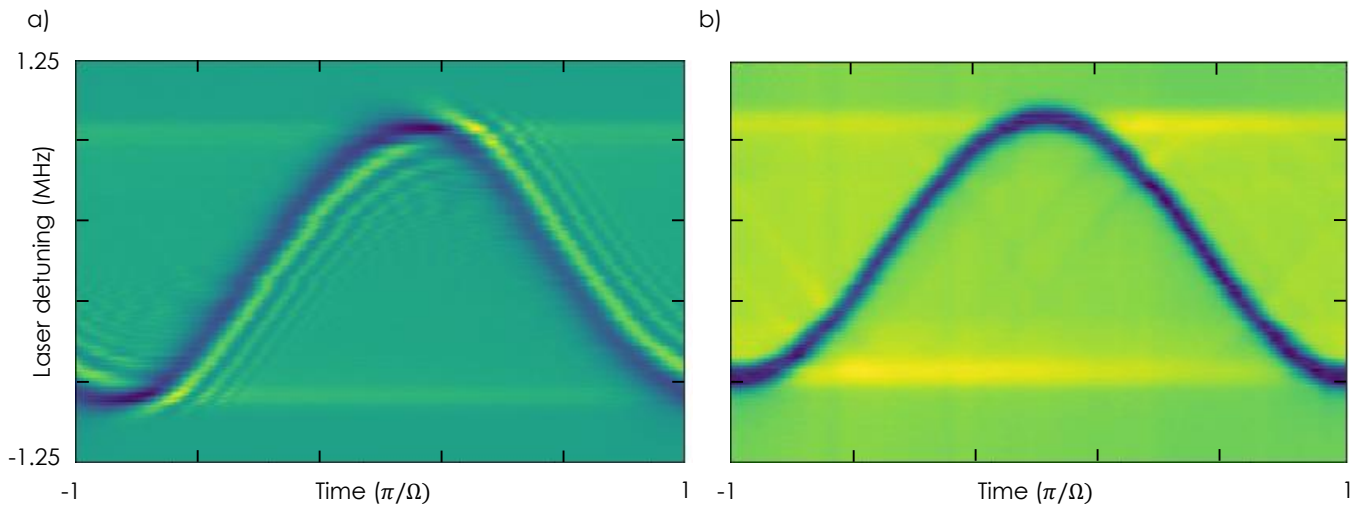


FIG. 6. Band dispersions obtained when calibrating the FSR with  $|\Omega' - \Omega| \approx 40 \text{ kHz}$  in (a) and  $|\Omega' - \Omega| < 2 \text{ kHz}$  in (b).

The FSR is the easiest frequency splitting to calibrate as it does not fluctuate significantly in time. Hence, it can be measured a single time prior to the experiment and be kept identical for all measurements. While a good first approximation can be made using the fact that  $\Omega = \frac{2\pi c}{nL}$ , this doesn't yield a precise enough value. To increase the precision, we send the following signals to the EOMs:

$$V^{(cw/ccw)}(t) = \frac{V_{nnn}}{2} e^{-i\Omega' t} + \text{c.c}$$

This results in the coupling of next-nearest-neighbours which are exactly split by a frequency  $\Omega$ . Since each sub-lattice is coupled independently by this driving field and that no coupling between sub-lattices is introduced, the effective



bands emerging from each frequency mode are identical and correspond to that of a lattice of identical sites with a unique hopping strength. This leads to band dispersions of the form:

$$\omega(t) = -2J'\cos(\Omega't).$$

A slight detuning between  $\Omega'$  and  $\Omega$  results, in the rotating frame, in a linearly varying frequency detuning between the drive and the frequency eigenmodes, and thus to an effective electric field. This effective field leads to asymmetric features with respect to  $k = 0$  in the measurement of the dispersion relation. Hence, we can tune  $\Omega'$  until we reach symmetric bands (Fig.6). This procedure can be further optimized by changing the modulation frequency to  $N\Omega$ , thus enhancing by a factor  $N$  the accuracy of the calibration. This led to a value of  $\Omega = 2\pi \times 6.628 \text{ MHz} \pm 1 \text{ kHz}$  with an uncertainty of less than 5 kHz when modulating up to  $N = 10$ .

## 2. Calibration of the sub-lattice spacing $\delta$

Calibration of the sub-lattice spacing  $\delta$  is much more challenging as thermal fluctuations continuously modify the relative length of the CW and CCW branches between the circulators, hence changing the frequency splitting between the hybridized modes on a timescale of the order of several hundreds ms. Moreover, for the Haldane model measurements, we need to work in a regime with a very specific detuning between CW and CCW modes such that the frequency eigenmodes in Eq. (3) of the Methods section have  $U \neq V$ . This allows modulating the two sub-lattices independently – using the modulators in the CW and CCW branches – which is a necessary requirement for engineering NNN couplings with opposite phase for the two sub-lattices. When implementing the Haldane model, we typically operate in a regime where  $|U|^2/|V|^2 \sim 20$  such that we can reach a phase difference close to  $\pi$  between the NNN couplings of the two sub-lattices, but still have significant NN couplings (which scale as  $UV$ ) with moderate EOM drive amplitude.

Hence, the challenge consists in fixing a specific and exact value of  $\delta$ , such that the the EOM drives do not induce undesirable variations of the effective on-site energies, while thermal fluctuations continuously modify the relative length of the CW and CCW branches hence continuously changing  $\delta_0$ .

To do this, we developed a two-step protocol that is implemented for every measurement realised in this work. This protocol consists in separating the acquisition process in two distinct time frames separated by 100 ms (which is typically faster than the typical thermal fluctuations rate); this dual-time-frame sequence repeats continuously with a period imposed by the low-bandwidth AWG which triggers all other electrical instruments. The first time frame is used to calibrate the value of  $\delta$  while the second is dedicated to the measurement itself. Each time frame has a duration of 50 ms during which the laser frequency scans a bandwidth comparable to the FSR in order to measure at least two band structures. During the first time frame used for calibration, the EOMs are driven with the following signal:

$$V_{nn}^{(cw/ccw)}(t) = \pm \frac{1}{2} V^{(0)} \left[ e^{-i\delta't} + e^{-i(\Omega-\delta')t} \right] + \text{c.c} \quad (11)$$

with  $+$  and  $-$  corresponding to the modulation of the CW and CCW modes respectively, and  $\Omega$  obtained following the procedure described above. This driving field induces a coupling between NN lattice sites with identical strength  $V^{(0)}$ . Upon such driving, the effective band structures follow the following dispersion:

$$\omega_{\pm}(t) = \mp \sqrt{2J(1 + \cos(ka)) + (\bar{\Delta}/2)^2} \quad (12)$$

where  $J$  is a coupling coefficient proportional to  $V^{(0)}$  and  $\bar{\Delta} = \delta' - \delta$  is the detuning between the driving frequency and the sub-lattice spacing (whose effect can be viewed as a staggered on-site potential).

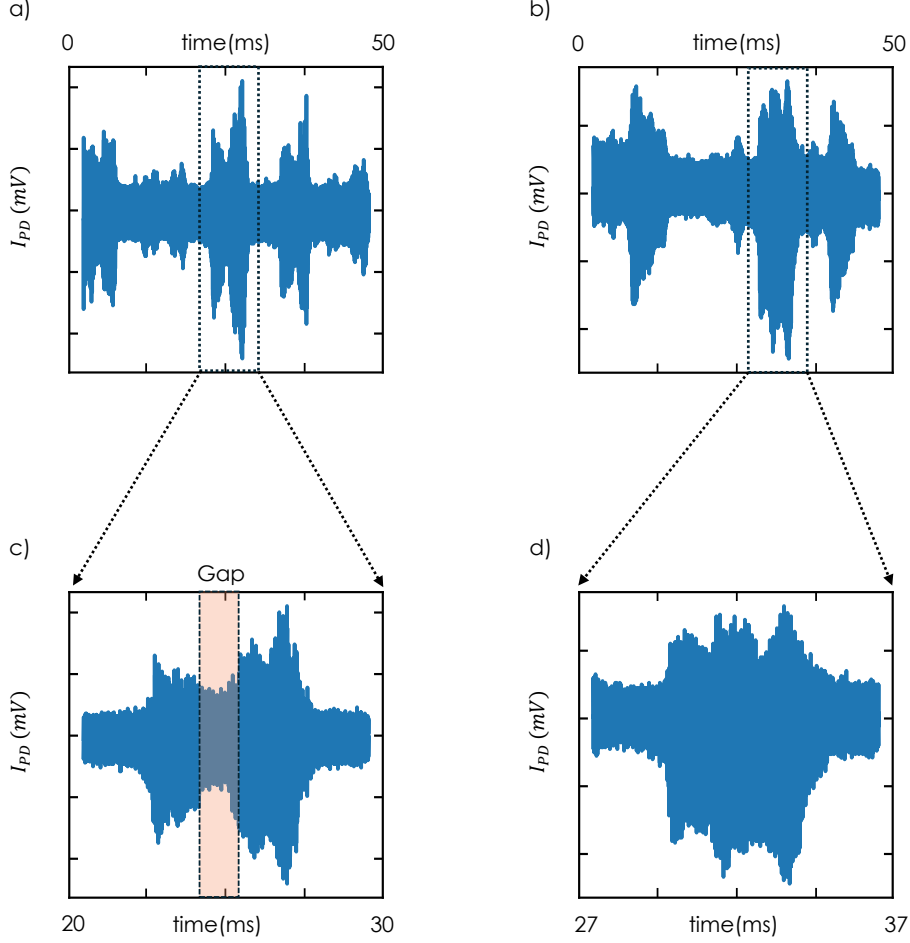


FIG. 7. Density of states can be observed visually from the transmission signal on both the digitizer and the oscilloscope when averaging the signal over a time-window much bigger than the period of a BZ. (a) shows densities of states that exhibit a gap and (c) is a zoom on one of them. This describes a regime where  $\delta' \neq \delta$ . Meanwhile, (b) depicts densities of states that are gapless, which can be more easily seen when zooming in (d). In this case, we have  $\delta' \approx \delta$  and we can acquire the data from the digitizer.

This dispersion relation is gapped whenever  $\bar{\Delta} \neq 0$ ; hence, probing the density of states (DOS) during this time frame (to identify moments where the DOS is not gapped) allows identifying when thermal fluctuations lead to  $\delta = \delta'$  (Fig. 7). Therefore, it is possible to define a value of  $\delta'$  with which we want to work and then wait until thermal fluctuations lead to a gapless DOS indicating perfect matching between the driving frequencies and the loop's eigenmode splitting, i.e.  $\bar{\Delta} = 0$ . Then, in the second time frame, the EOMs are driven with the fields described in the main text for each experimental part, using  $\delta'$  as the definition of the sub-lattice spacing. For graphene-like and hBN-like measurements,  $\delta'$  is chosen such that the CW and CCW modes are degenerate, i.e.  $\delta_0 = 0$ . This is because these models don't require NNN couplings. However, to implement the Haldane model,  $\delta'$  is chosen such that  $\delta_0 \approx 1.1$  MHz. This corresponds to values of  $|U| = 0.82$  and  $|V| = 0.18$ ; a regime where  $|U|^2/|V|^2 \sim 20$ .

More in specific, the procedure for acquiring data exactly when  $\bar{\Delta} = 0$  is the following. The electrical response from the photodiode measuring the transmitted signal is split in half with one part going to the oscilloscope and the other to the digitizer (see above section on the electrical setup). We ensure that the time delays for triggering the scope and the digitizer are such that the former acquires signal during the first time frame while the latter acquires during the second time frame; separating the signal in two distinct time windows ensures a high temporal resolution for each measurement. As soon as we observe a gapless density of states on the oscilloscope, we stop the acquisition which automatically transfers the memory buffer of the digitizer (containing the experimental signal measured upon good experimental conditions) to a computer where it can be analysed as described below.

## B. Band Structure Measurements

The band structures shown in figure 2 of the main text are obtained by modulating the laser frequency with a staircase triangular waveform with frequency 10 Hz and amplitude 0.075 V. Upon this modulation, we probe 50 ms time-windows (as described in the calibration procedure), each time-window corresponding to the descending part of a modulation period. These modulation parameters allow the scan of around one FSR of the optical fibre loop. Each step of the staircase has a duration of 130  $\mu$ s during which the laser frequency is kept constant. After the beginning of each laser step, we wait  $\sim 5$   $\mu$ s in order for the system to reach a steady-state before acquiring data.

The coupling between the different frequency eigenmodes that underlies the synthetic dimension scheme is ensured by driving the EOMs with a signal formed from Fourier components with frequencies equal to the frequency splittings between each pairs of modes to be coupled and amplitudes proportional to the corresponding hopping amplitude. The general formula describing the signal sent to the EOMs is the following:

$$V^{(cw/ccw)}(t) = \pm \frac{1}{2} [V_{nn}^{(1)} e^{-i\delta t} + V_{nn}^{(2)} e^{-i((\Omega-\delta)t + \phi_{shift})} + V_{nn}^{(3)} e^{-i(10\Omega + \delta)t}] + \frac{V_{n nn}}{2} e^{-i(\Omega t \pm \phi_h)} + \text{c.c} \quad (13)$$

with + and - corresponding to the modulation of the CW and CCW modes respectively. Specifically,  $V_{nn}^{(i)}$  with  $i = 1, 2, 3$  represent the nearest-neighbour hoppings of the honeycomb lattice; in particular the coupling  $V_{nn}^{(3)}$  to the 21<sup>st</sup> neighbour is used to simulate the second dimension. Components  $V_{n nn}$  are linked to the next-nearest-neighbour hoppings of the Haldane model;  $V_{n nn}$  is taken to be zero when emulating graphene-like and hBN-like Hamiltonians.

Throughout each frequency step of the laser scan, we measure the time-resolved transmitted signal with a high-bandwidth photodiode. The arrival time of the photons can be mapped to a two-dimensional Brillouin zone (BZ) using the relations (see the derivation in the following section):

$$\begin{aligned} t &\mapsto (k_x, k_y) \\ k_x &= t - \frac{2\pi\phi_{shift}}{10\Omega} \pmod{\frac{2\pi}{\Omega}} \\ k_y &= t \pmod{\frac{2\pi}{10\Omega}}. \end{aligned} \quad (14)$$

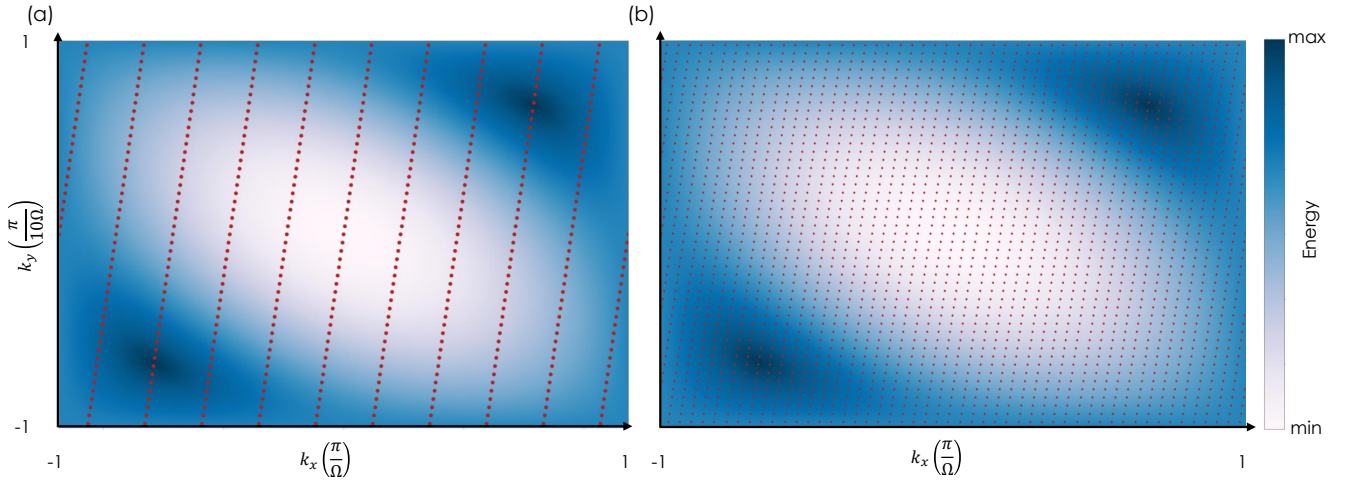


FIG. 8. Points sampled on the complete 2D BZ. The colorplot in the background shows the theoretical dispersion of the lower band for graphene. The points sampled by using a single value of  $\phi_{shift}$  value are depicted with red dots in (a) and the combined sampling using 5 different values of  $\phi_{shift}$  is shown in (b).

Hence, the effective BZ in the time domain has periodicity  $\frac{2\pi}{\Omega}$  along  $k_x$  and  $\frac{2\pi}{10\Omega}$  along  $k_y$ . The measurement of intensity dips at time  $t$  indicates that the laser is resonant with an eigenmode with effective crystal momentum  $\mathbf{k} = (k_x, k_y)$ . Moreover, the effect of adding a phase  $\phi_{shift}$  to the Fourier component  $V_{nn}^{(2)}$  results in a shift of the definition of  $k_x$ . This allows the time trace monitored on the photodiode to follow horizontally shifted trajectories in reciprocal space. This is best seen by considering the mapping of the time bins of each measurement on the

photodiode onto the BZ: this is presented in Fig. 8 (a) for  $\phi_{shift} = 0$  (each red dot represents a single time bin with a time separation dictated by the sampling rate of the digitizer), and in Fig. 8 (b) for 5 distinct values  $\phi_{shift} = 1.25 \frac{\pi}{10}, 0.625 \frac{\pi}{10}, 0, -0.625 \frac{\pi}{10}, -1.25 \frac{\pi}{10}$ . In order to obtain such a denser covering of the Brillouin zone, the EOM signal through each laser frequency step is partitioned in 5 equally spaced time regions, separated by  $3 \mu\text{s}$  and lasting the equivalent of 150 BZs. In each region, the EOM signal has one specific value of the phase  $\phi_{shift}$  among the 5 ones used in Fig. 8 (b). A schematic of the pulse sequence used is depicted in Fig. 9; a burst signal is also generated by the HDAWG at the beginning of each laser step and monitored on the digitizer to ensure that we can precisely identify the temporal position of each laser step in our data analysis.

For each  $\phi_{shift}$  region of each laser step, we average the photodiode signal over the 150 trajectories through the BZ to obtain a single trajectory across the BZ with a high signal-to-noise ratio. Then, by scanning the laser frequency and vertically stacking these averaged signals measured at each step, we can construct the full band structure. Figure 2 (a), (e), (g) of the main text show this construction when stacking only the signal associated to the region with  $\phi_{shift} = 0$ . Figure 2 (c) of the main text presents the value of the lower band energy measured at each time bin in Fig. 8 (b). Finally, Fig. 2 (d), (f), (h) of the main text present the data measured at specific time bins along the high-symmetry trajectory  $M - K - \Gamma - M$ .

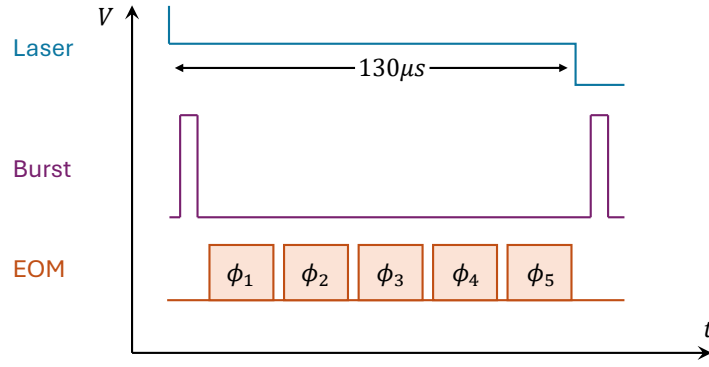


FIG. 9. Electrical signals sent to modulate the frequency of the laser (blue), the EOMs (orange), and sent directly to the digitizer (purple) to realize band structure measurements.

### C. Berry Curvature measurement

To obtain the Berry curvatures shown in figure 3 of the main text, we use the same data points as for the band structure measurements. Indeed, the transmission intensity measured by the photodiode is given by (see derivation in theoretical framework):

$$\begin{aligned}
 1 - \frac{I_{pd}^+}{|F|^2} &\approx 2\kappa \operatorname{Re} \left\{ \frac{U^2 \cos^2 \left( \frac{\theta_{\mathbf{k}}}{2} \right) + \frac{UV}{2} \sin(\theta_{\mathbf{k}}) e^{-i\delta t} e^{i\phi_{\mathbf{k}}}}{\frac{\gamma}{2} - i(\Delta\omega_L - \epsilon_{\mathbf{k}}^+)} \right\} \Big|_{(k_x, k_y) = (t \bmod T, t \bmod T')} \\
 1 - \frac{I_{pd}^-}{|F|^2} &\approx 2\kappa \operatorname{Re} \left\{ \frac{U^2 \sin^2 \left( \frac{\theta_{\mathbf{k}}}{2} \right) - \frac{UV}{2} \sin(\theta_{\mathbf{k}}) e^{-i\delta t} e^{i\phi_{\mathbf{k}}}}{\frac{\gamma}{2} - i(\Delta\omega_L - \epsilon_{\mathbf{k}}^-)} \right\} \Big|_{(k_x, k_y) = (t \bmod T, t \bmod T')}
 \end{aligned} \tag{15}$$

where  $I_{pd}^{\pm}$  is the intensity measured by the photodiode with respect to the lower (+) and upper (-) band,  $\kappa$  is the input-output coupling strength that quantifies the radiative loss rate,  $\Delta\omega_L$  is the difference in angular frequency between the driven input field and the  $\bar{m}$ th-symmetric mode, which we assume to be the closest to the input field,  $\epsilon_{\mathbf{k}}^{\pm}$  is the energy of the lower(+) and upper(-) band, and  $\phi_{\mathbf{k}}$  and  $\theta_{\mathbf{k}}$  are the polar and azimuthal angles parametrizing the eigenstates. Therefore, by using complementary methods, we can experimentally extract both  $\phi_{\mathbf{k}}$  and  $\theta_{\mathbf{k}}$  from the transmission signal.



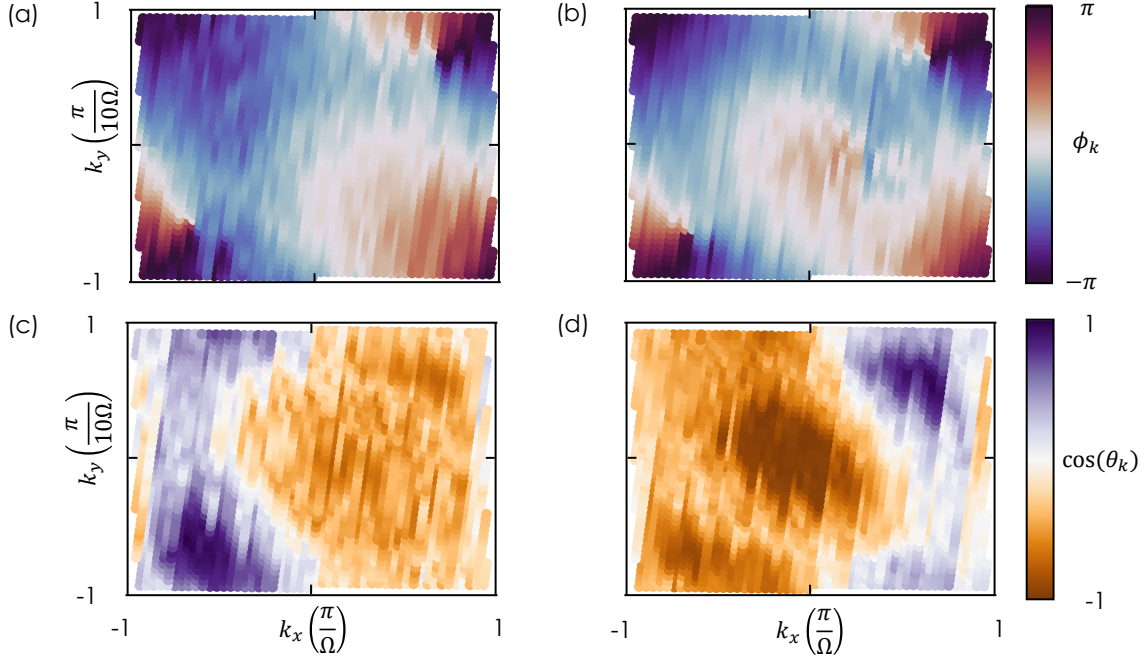


FIG. 10. 2D Mapping of extracted phases  $\phi_{\mathbf{k}}$  and  $\theta_{\mathbf{k}}$  that are used in figure 3 of main text for the Haldane model datasets with  $\phi_h = \pm \frac{\pi}{2}$ . (a) and (b) show the mapping of  $\phi_{\mathbf{k}}$  for  $\phi_h = +\frac{\pi}{2}$  and  $\phi_h = -\frac{\pi}{2}$  respectively, whereas (c) and (d) show the mapping of  $\cos(\theta_{\mathbf{k}})$  with respect to the same data as (a) and (b) respectively.

### 1. Extraction of $\phi_{\mathbf{k}}$

The extraction of  $\phi_{\mathbf{k}}$  is realised using the procedure introduced in Ref. [34]. Let us assume we want to extract  $\phi_{\mathbf{k}}$  for the lower band. Equations 15 show that the transmitted intensity ( $I_{pd}^+$ ) is time-modulated with frequency  $\delta$  and phase  $\phi_{\mathbf{k}}$ . Specifically, each of the 150 BZs on a given laser step will have transmission peaks happening at the same times with respect to the start of each BZ, but these peaks will not have the same amplitude between different BZs.

Hence, for each  $\mathbf{k}$ -point, we want to measure how the transmitted intensity varies over the different BZ, and extract the phase of this modulation. To obtain a precise value of the transmitted intensity at each time bin corresponding to a given  $\mathbf{k}$ -point, we sum the intensity measured at this specific time bin (with respect to the beginning of the step) over all the laser steps covering the lower band; this corresponds to integrating the measured signal for a given time bin over each laser detuning. This allows properly taking into account the spectral linewidth of each eigenmode. Then, for every  $\mathbf{k}$ -point we evaluate how the transmitted intensity varies over the different BZs by taking the Fourier component at  $\delta$  of the signal created from juxtaposing the 150 different intensity values measured at time bins corresponding to this  $\mathbf{k}$ -point. Taking the argument of this demodulated signal at every  $\mathbf{k}$  yields  $\phi_{\mathbf{k}}$ .

Examples of the extraction of  $\phi_{\mathbf{k}}$  for the Haldane model (presented in Fig. 3 of the main text) are presented in Fig. 10 (a) and (b).

### 2. Extraction of $\theta_{\mathbf{k}}$

To extract  $\theta_{\mathbf{k}}$ , we now consider the time-integrated transmitted intensity over the 150 BZs that is used in the band structure measurements. Doing so, the time-dependent oscillation at frequency  $\delta$  averages out and the integrated dip in the transmitted intensity, when the frequency of the driven input field is resonant to the energy of a band, is given by:

$$\begin{aligned}
 T^+ &\equiv 1 - \frac{I_{pd}^+}{|F|^2} \approx 4\kappa \frac{U^2 \cos^2\left(\frac{\theta_{\mathbf{k}}}{2}\right)}{\gamma} \\
 T^- &\equiv 1 - \frac{I_{pd}^-}{|F|^2} \approx 4\kappa \frac{U^2 \sin^2\left(\frac{\theta_{\mathbf{k}}}{2}\right)}{\gamma}.
 \end{aligned} \tag{16}$$

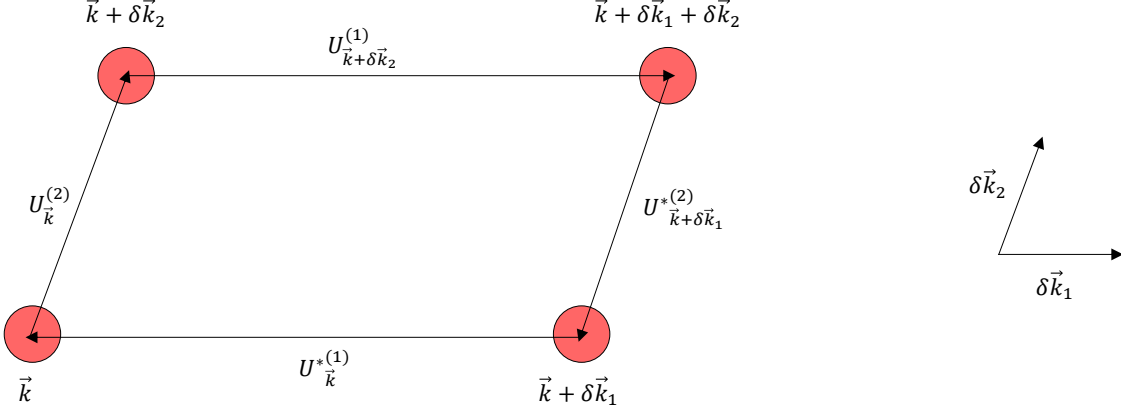


FIG. 11. Schematic representation of the plaquette considered in the extraction of  $\Omega_{\mathbf{k}}$ . The red circles represent sampled points.

Then, we consider the difference between the intensities of the two bands, normalized by their sum:

$$\begin{aligned}
 \frac{T^+ - T^-}{T^+ + T^-} &= \frac{4\kappa U^2}{\gamma} \frac{(\cos^2(\frac{\theta_{\mathbf{k}}}{2}) - \sin^2(\frac{\theta_{\mathbf{k}}}{2}))}{(\cos^2(\frac{\theta_{\mathbf{k}}}{2}) + \sin^2(\frac{\theta_{\mathbf{k}}}{2}))} \\
 &= \cos^2\left(\frac{\theta_{\mathbf{k}}}{2}\right) - \sin^2\left(\frac{\theta_{\mathbf{k}}}{2}\right) \\
 &= \cos(\theta_{\mathbf{k}}).
 \end{aligned} \tag{17}$$

Hence, we have that  $\arccos\left(\frac{T^+ - T^-}{T^+ + T^-}\right) = \theta_{\mathbf{k}}$ .

Examples of the extraction of  $\cos(\theta_{\mathbf{k}})$  for the Haldane model (presented in Fig. 3 of the main text) are presented in Fig. 10 (c) and (d).

### 3. Mapping on the Bloch sphere

Once we have extracted both polar and azimuthal angles using the methods described above, it is very straightforward to map the eigenstates on a Bloch sphere. The order with which the different points cover the Bloch sphere is chosen to be the ordering of all the points with respect to their value of  $k_x$ .

### 4. Extraction of the Berry curvature

The expression for the Berry curvature is defined as:

$$\Omega_{\mathbf{k}} = \nabla_{\mathbf{k}} \times \langle \psi_{\mathbf{k}} | i \nabla_{\mathbf{k}} | \psi_{\mathbf{k}} \rangle \tag{18}$$

with  $|\psi_{\mathbf{k}}\rangle = \cos\left(\frac{\theta_{\mathbf{k}}}{2}\right)|a\rangle + \sin\left(\frac{\theta_{\mathbf{k}}}{2}\right)e^{i\phi_{\mathbf{k}}}|b\rangle$ . This is difficult to evaluate from experimental data as it involves numerical derivatives over a discrete number of points presenting experimental fluctuations. Instead, we use a technique developed by Fukui et al.[36] for discretized BZs. We first consider the following quantity:

$$U_{\mathbf{k}}^{(\mu)} = \frac{\langle \psi_{\mathbf{k}} | \psi_{\mathbf{k} + \delta \mathbf{k}_{\mu}} \rangle}{|\langle \psi_{\mathbf{k}} | \psi_{\mathbf{k} + \delta \mathbf{k}_{\mu}} \rangle|} \tag{19}$$

with  $\mathbf{k}$  a discrete point sampled in the BZ (here a specific time bin) and  $\delta \mathbf{k}_{\mu}$  the vectors linking adjacent  $\mathbf{k}$ -points.

This quantity is easy to calculate at each  $\mathbf{k}$  as we have extracted both polar and azimuthal angles at each point; thus, we know the eigenstate at each  $\mathbf{k}$ .

We can then refer to the 2D mapping described previously to determine the distribution of the  $\mathbf{k}$ -points sampled across the BZ, partition this latter into plaquettes, and identify the pairs of  $\mathbf{k}$ -points for which the scalar products have to be calculated.

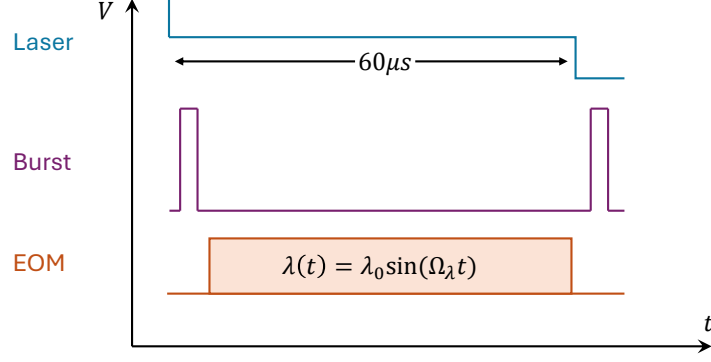


FIG. 12. Electrical signals send to modulate the frequency of the laser(blue), to modulate the EOMs(orange), and sent directly to the digitizer(purple) to realize anomalous displacement measurements.

The Berry curvature flux through a plaquette is given by:

$$\Omega_{\mathbf{k}} = \frac{1}{i} \ln \left[ U_{\mathbf{k}}^{(2)} U_{\mathbf{k}+\delta\mathbf{k}_2}^{(1)} U_{\mathbf{k}+\delta\mathbf{k}_1}^{*(2)} U_{\mathbf{k}}^{*(1)} \right] \quad (20)$$

where the plaquette described by this equation is schematically shown in fig 11. Finally, the Chern number is then simply obtained by summing the extracted Berry curvature over all plaquettes forming the BZ:

$$\mathcal{C} = \frac{1}{2\pi} \sum_{\mathbf{k} \in \text{BZ}} \Omega_{\mathbf{k}}. \quad (21)$$

#### D. Anomalous Transverse Displacement

To obtain anomalous transverse displacement measurements, we slightly change the signals sent to the laser and to the EOMs. The laser frequency is now modulated by a staircase triangular waveform of frequency 20 Hz and amplitude 0.075 V, with steps of 60  $\mu\text{s}$  (see Fig. 12). The general formula describing the signal sent to the EOMs is now the following:

$$V^{(cw/ccw)}(t) = \pm \frac{1}{2} [V_{nn}^{(1)} e^{-i\delta t} + V_{nn}^{(2)} e^{-i((\Omega-\delta)t)} + V_{nn}^{(3)} e^{-i(10\Omega+\delta+\lambda_t)t}] + \frac{V_{nnn}}{2} e^{-i(\Omega t \pm \phi_n)} + \text{c.c.} \quad (22)$$

where  $\lambda_t = \lambda_0 \sin(\Omega_\lambda t)$  simulates an oscillating electric potential  $V = \lambda_t y$  with amplitude  $\lambda_0 = 10$  kHz and frequency  $\Omega_\lambda = 100$  kHz. This acts as a uniform electric field on the lattice:

$$E = -\nabla V = -\lambda_t \hat{y}. \quad (23)$$

In contrast with the band structure measurements, the EOM signal is now partitioned into a single time frame lasting the equivalent of 370 BZs per laser step. Through each of these frequency steps scanned by the laser, we now consider the time-resolved heterodyne signal measured with two high-bandwidth photodiode; each probing the signal radiating from either direction from the output coupler shown in Fig 5. Each of these heterodyne signals are then split into different time windows of 1  $\mu\text{s}$  associated to a time value  $t_n$  (see Fig. 13). For each time window, the Fourier transform gives a spectrum centred at  $\omega_0/2\pi = 200$  MHz - the frequency of the LO - with peaks corresponding to the locations of the supermodes in the frequency space. We then define the displacement for a given  $t_n$  as:

$$\langle \Delta x \rangle (t_n) = \sum_{\omega} \frac{(\omega - \omega_0) I_{\omega}}{\sum_{\omega} I_{\omega}} \quad (24)$$

with  $I_{\omega}$  the intensity of a given mode. Redoing this for each time window yields a time-dependent displacement  $\langle x \rangle (t)$ . We then demodulate this displacement with respect to the oscillating electric field's frequency :

$$\langle \Delta x \rangle = \frac{1}{\xi} \int_0^{60 \mu\text{s}} dt \langle \Delta x \rangle (t) \sin(\Omega_\lambda t) \quad (25)$$

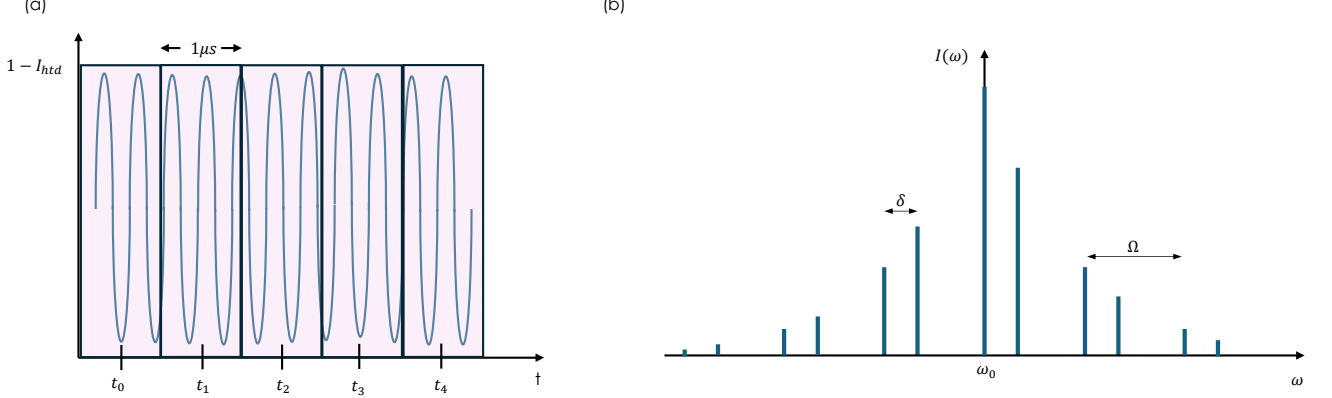


FIG. 13. Schematic representation of the windowed Fourier transform process to measure the anomalous displacement. (a) depicts the partitioning of the heterodyne signal into different time windows, with the Fourier transform of a given window shown in (b).

where  $\xi = \int_0^{60 \mu\text{s}} dt \sin^2(\Omega_\lambda t)$  is a normalization constant. Repeating this process for every laser frequency step gives the results shown in Fig. 4 of the main text. We then extract the Chern number for a given band straightforwardly using (see theoretical frameworks for derivation):

$$\mathcal{C} = -\frac{\gamma^2}{4\pi^2 \lambda_0} \int_{\text{band}} d\omega_L \langle \Delta x \rangle_{\omega_L} \int \frac{d^2 \mathbf{k}}{(\epsilon_{\mathbf{k}} - \omega_L)^2 + (\gamma/2)^2} \quad (26)$$

where  $\omega_L$  is the frequency corresponding to a step of the laser scan and the integral is performed across the spectral width of the band of interest;  $\gamma$  is the average linewidth of the band which is obtained by measuring the full width at half maximum (FWHM) at  $\mathbf{k}$ -points where the band dispersion reaches an extremum and averaging these values;  $\epsilon_{\mathbf{k}}$  is the energy of the band; and  $\langle \Delta x \rangle_{\omega_L}$  is the displacement measured above for a given laser step divided by  $\Omega$ , so to have displacements in units of the unit cell size. Finally, the integral over  $d^2 \mathbf{k}$  is done experimentally by the change of variable  $d^2 \mathbf{k} = 2\pi\Omega d\tau$ , where  $d\tau = 320 \text{ ps}$  is the digitizer's sampling rate (in this equation,  $\mathbf{k}$  is dimensionless as it is defined for a normalized unit cell).

To measure the uncertainty on these extracted Chern numbers, we first calculate the variance in the displacement for graphene-like lattice in fig. 4(e) of main text. As we expect a theoretical transverse drift of 0 for this model, the variance in this measurement characterizes the uncertainty on the measured transverse displacement for each model. Then, we propagate this uncertainty by injecting the value found for the variance into eq (26). Finally, taking the square root of this yields the propagated standard deviation, which in this measurement is found to be an uncertainty of  $\pm 0.10$ .

## IV. THEORETICAL FRAMEWORK

### A. Derivation of the Haldane Hamiltonian

The Hamiltonian describing the effect of the EOMs is given by:

$$\begin{aligned} H_{EOM} &= H_{CW} + H_{CCW} \\ &= 2\eta \sum_{m,n} \left[ V_{CW}(t) d_{m,\downarrow}^\dagger d_{n,\downarrow} e^{2i\pi(n-m)\frac{l_{CW}}{L}} + V_{CCW}(t) d_{m,\uparrow}^\dagger d_{n,\uparrow} e^{2i\pi(n-m)\frac{l_{CCW}}{L}} \right] \end{aligned} \quad (27)$$

with  $d_{m,\downarrow}$ ,  $d_{m,\uparrow}$  the bosonic operators associated to the  $m$ -th CW and CCW modes,  $l_{CW}$  and  $l_{CCW}$  the position of the CW and CCW modulators with respect to the start of the loop, and  $\eta$  the electro-optics coupling coefficient. We



will pose  $l_{CW} = l_{CCW} = \frac{l}{2}$  as the change of length due to thermal fluctuations ( $\sim 1 \mu\text{m}$ ) is negligible with respect to the total length of the cavity ( $\sim 40 \text{ m}$ ). The expression for the Hamiltonian therefore becomes:

$$H_{EOM} = 2\eta \sum_{m,n} (-1)^{n-m} \left[ V_{CW}(t) d_{m,\downarrow}^\dagger d_{n,\downarrow} + V_{CCW}(t) d_{m,\uparrow}^\dagger d_{n,\uparrow} \right]. \quad (28)$$

We then define the operators associated to the coupled basis:

$$\begin{aligned} a_m &= U d_{m,\uparrow} + V d_{m,\downarrow} \\ b_m &= V d_{m,\uparrow} - U d_{m,\downarrow} \end{aligned} \quad (29)$$

where we choose, without loss of generality, a gauge where  $U, V \in \mathbb{R}$ . In this basis, the Hamiltonian becomes:

$$\begin{aligned} H_{EOM} &= 2\eta \sum_{m,n} (-1)^{n-m} \left[ V_{CW}(t) (V a_m^\dagger - U b_m^\dagger) (V a_n - U b_n) + V_{CCW}(t) (U a_m^\dagger + V b_m^\dagger) (U a_n + V b_n) \right] \\ &= 2\eta \sum_{m,n} (-1)^{n-m} \left[ V_{CW}(t) (V^2 a_m^\dagger a_n + U^2 b_m^\dagger b_n - UV (a_m^\dagger b_n + b_m^\dagger a_n)) \right] \\ &\quad + 2\eta \sum_{m,n} (-1)^{n-m} \left[ V_{CCW}(t) (U^2 a_m^\dagger a_n + V^2 b_m^\dagger b_n + UV (a_m^\dagger b_n + b_m^\dagger a_n)) \right]. \end{aligned} \quad (30)$$

Let us now consider the effect of the NN and NNN couplings separately by posing

$$\begin{aligned} V_{CW}(t) &= V_{NN}(t) + V_{NNN}^{CW}(t) \\ V_{CCW}(t) &= -V_{NN}(t) + V_{NNN}^{CCW}(t) \end{aligned} \quad (31)$$

such that

$$H_{EOM} = H_{NN} + H_{NNN}. \quad (32)$$

### 1. Derivation of the NN Hamiltonian

Let us first look at the NN couplings:

$$H_{NN} = -2\eta V_{NN}(t) \sum_{m,n} (-1)^{n-m} \left[ (U^2 - V^2) (a_m^\dagger a_n - b_m^\dagger b_n) + 2UV (a_m^\dagger b_n + b_m^\dagger a_n) \right]. \quad (33)$$

We then move to the rotating frame using:

$$\begin{aligned} \tilde{a}_m &= a_m e^{i(m\Omega - \frac{\delta}{2})t} \\ \tilde{b}_m &= b_m e^{i(m\Omega + \frac{\delta}{2})t} \end{aligned} \quad (34)$$

The Hamiltonian becomes:

$$\tilde{H}_{NN} = -2\eta V_{NN}(t) \sum_{m,n} (-1)^{n-m} e^{-i(n-m)\Omega t} \left[ (U^2 - V^2) (\tilde{a}_m^\dagger \tilde{a}_n - \tilde{b}_m^\dagger \tilde{b}_n) + 2UV (e^{-i\delta t} \tilde{a}_m^\dagger \tilde{b}_n + e^{i\delta t} \tilde{b}_m^\dagger \tilde{a}_n) \right]. \quad (35)$$

We then define

$$V_{NN}(t) = \left[ \frac{V_{NN}^{(0)}}{2} e^{-i(\delta+\Delta)t} + \frac{V_{NN}^{(1)}}{2} e^{-i(\Omega-\delta-\Delta)t} + \frac{V_{NN}^{(2)}}{2} e^{-i(10\Omega+\delta+\Delta)t} \right] + \text{c.c.} \quad (36)$$

Injecting this expression in the Hamiltonian and using the Rotating Wave Approximation to neglect fast-oscillating terms, we obtain:

$$\begin{aligned} \tilde{H}_{NN} &= -2\eta UV \sum_m \left[ V_{NN}^{(0)} (e^{-i\Delta t} \tilde{b}_m^\dagger \tilde{a}_m + e^{i\Delta t} \tilde{a}_m^\dagger \tilde{b}_m) - V_{NN}^{(1)} (e^{-i\Delta t} \tilde{b}_{m-1}^\dagger \tilde{a}_m + e^{i\Delta t} \tilde{a}_m^\dagger \tilde{b}_{m-1}) \right. \\ &\quad \left. + V_{NN}^{(2)} (e^{-i\Delta t} \tilde{b}_m^\dagger \tilde{a}_{m-10} + e^{i\Delta t} \tilde{a}_{m-10}^\dagger \tilde{b}_m) \right] \end{aligned} \quad (37)$$

Under a gauge transformation (see Ref. [64]):

$$\begin{aligned}\tilde{a}_m &\rightarrow \tilde{a}_m e^{-i\frac{\Delta}{2}t} \\ \tilde{b}_m &\rightarrow \tilde{b}_m e^{i\frac{\Delta}{2}t}\end{aligned}\quad (38)$$

we obtain the following equivalent Hamiltonian:

$$\begin{aligned}\tilde{H}_{NN} &= \frac{\Delta}{2} \sum_m \left[ \tilde{a}_m^\dagger \tilde{a}_m - \tilde{b}_m^\dagger \tilde{b}_m \right] \\ &\quad - 2\eta UV \sum_m \left[ V_{NN}^{(0)} (\tilde{b}_m^\dagger \tilde{a}_m + \tilde{a}_m^\dagger \tilde{b}_m) - V_{NN}^{(1)} (\tilde{b}_{m-1}^\dagger \tilde{a}_m + \tilde{a}_m^\dagger \tilde{b}_{m-1}) \right. \\ &\quad \left. + V_{NN}^{(2)} (\tilde{b}_m^\dagger \tilde{a}_{m-10} + \tilde{a}_{m-10}^\dagger \tilde{b}_m) \right].\end{aligned}\quad (39)$$

Using the periodicity of our system, we can move to reciprocal space using

$$\begin{aligned}\tilde{a}_m &= \int_0^T \frac{dk_x}{T} \int_0^{T'} \frac{dk_y}{T'} e^{im(k_x\Omega + k_y\Omega)} a_{\mathbf{k}} \\ \tilde{b}_m &= \int_0^T \frac{dk_x}{T} \int_0^{T'} \frac{dk_y}{T'} e^{im(k_x\Omega + k_y\Omega)} b_{\mathbf{k}}\end{aligned}\quad (40)$$

where  $T = \frac{2\pi}{\Omega}$ ,  $T' = \frac{2\pi}{10\Omega}$ , and  $k_{x,y}$  are effective crystal momenta with units of time and periodicity of  $T$  and  $T'$  respectively. This reflects the  $\Omega$  and  $10\Omega$  periodicity of the effective lattice along  $x$  and  $y$  respectively and yields the following Hamiltonian in momentum space:

$$H_{NN}(\mathbf{k}) = \int_0^T \frac{dk_x}{T} \int_0^{T'} \frac{dk_y}{T'} \left[ \frac{\Delta}{4} (a_{\mathbf{k}}^\dagger a_{\mathbf{k}} - b_{\mathbf{k}}^\dagger b_{\mathbf{k}}) - 2\eta UV \left( V_{NN}^{(0)} - V_{NN}^{(1)} e^{ik_x\Omega} + V_{NN}^{(2)} e^{-10ik_y\Omega} \right) b_{\mathbf{k}}^\dagger a_{\mathbf{k}} \right] + \mathbf{h} \cdot \mathbf{c} \quad (41)$$

where we have used the definition of a Dirac comb

$$D_T(t-a) = \frac{1}{T} \sum_m e^{i\left(\frac{2\pi}{T}\right)m(t-a)} \quad (42)$$

to simplify the expression. This Hamiltonian can then be written in matrix form:

$$H_{NN}(\mathbf{k}) = \int_0^T \frac{dk_x}{T} \int_0^{T'} \frac{dk_y}{T'} \psi_{\mathbf{k}}^\dagger \cdot h_{NN}(\mathbf{k}) \cdot \psi_{\mathbf{k}} \quad (43)$$

$$h_{NN}(\mathbf{k}) = \begin{bmatrix} -\frac{\Delta}{2} & g(\mathbf{k}) \\ g^*(\mathbf{k}) & \frac{\Delta}{2} \end{bmatrix}; \psi_{\mathbf{k}} = \begin{bmatrix} b_{\mathbf{k}} \\ a_{\mathbf{k}} \end{bmatrix} \quad (44)$$

with  $g(\mathbf{k}) = -2\eta UV \left( V_{NN}^{(0)} - V_{NN}^{(1)} e^{ik_x\Omega} + V_{NN}^{(2)} e^{-10ik_y\Omega} \right)$ .

This correctly describes the Hamiltonian of a particle hopping on a honeycomb lattice in the brickwall geometry with  $\Delta$  providing a constant mass term.

## 2. Derivation of the NNN Hamiltonian

We will now consider the effect of the NNN couplings:

$$\begin{aligned}H_{NNN} &= 2\eta \sum_{m,n} (-1)^{n-m} \left[ V_{NNN}^{CW}(t) (V^2 a_m^\dagger a_n + U^2 b_m^\dagger b_n - UV (a_m^\dagger b_n + b_m^\dagger a_n)) \right. \\ &\quad \left. + V_{NNN}^{CCW}(t) (U^2 a_m^\dagger a_n + V^2 b_m^\dagger b_n + UV (a_m^\dagger b_n + b_m^\dagger a_n)) \right].\end{aligned}\quad (45)$$

We move to the rotating frame:

$$\begin{aligned}\tilde{H}_{NNN} &= 2\eta \sum_{m,n} (-1)^{n-m} e^{-i(n-m)\Omega t} \left[ V_{NNN}^{CW}(t) \left( V^2 \tilde{a}_m^\dagger \tilde{a}_n + U^2 \tilde{b}_m^\dagger \tilde{b}_n - UV \left( e^{-i\delta t} \tilde{a}_m^\dagger \tilde{b}_n + e^{i\delta t} \tilde{b}_m^\dagger \tilde{a}_n \right) \right) \right. \\ &\quad \left. + V_{NNN}^{CCW}(t) \left( U^2 \tilde{a}_m^\dagger \tilde{a}_n + V^2 \tilde{b}_m^\dagger \tilde{b}_n + UV \left( e^{-i\delta t} \tilde{a}_m^\dagger \tilde{b}_n + e^{i\delta t} \tilde{b}_m^\dagger \tilde{a}_n \right) \right) \right].\end{aligned}\quad (46)$$

We then define:

$$\begin{aligned} V_{NNN}^{CW}(t) &= \frac{V_{NNN}}{2} e^{-i(\Omega t + \phi_h)} + \mathbf{c.c.} \\ V_{NNN}^{CCW}(t) &= \frac{V_{NNN}}{2} e^{-i(\Omega t - \phi_h)} + \mathbf{c.c.} \end{aligned} \quad (47)$$

Substituting these relations in the expression of the Hamiltonian and once again using the Rotating Wave Approximation to neglect fast oscillating terms, we get:

$$\tilde{H}_{NNN} = -\eta V_{NNN} \sum_m \left[ (V^2 e^{i\phi_h} + U^2 e^{-i\phi_h}) \tilde{a}_m^\dagger \tilde{a}_{m-1} + (U^2 e^{i\phi_h} + V^2 e^{-i\phi_h}) \tilde{b}_m^\dagger \tilde{b}_{m-1} \right] + \mathbf{h.c.} \quad (48)$$

This expression highlights a feature that is crucial to our implementation of the Haldane model: while the NN hoppings between different  $a, b$  sublattices described in (39) are all proportional to  $UV$ , the different NNN hoppings included in  $\tilde{H}_{NNN}$  involve different combinations of  $U^2$  and  $V^2$  and, thus, can have different NNN hopping phases for the  $a$  and  $b$  sublattices as required to realize the simplified Haldane model. In physical terms, the fact that the  $a$  ( $b$ ) sublattices involve a majority of CCW (CW)-propagating light allows to selectively address them in spite of the frequency difference being the same  $\Omega$ : their hopping is in fact mostly determined by the modulation applied to the EOM located in the corresponding CCW (CW) branch, which can be individually controlled.

Going into reciprocal space and using the definition of a Dirac comb to simplify the expression, this becomes:

$$\begin{aligned} H_{NNN}(\mathbf{k}) &= -\eta V_{NNN} \int_0^T \frac{dk_x}{T} \int_0^{T'} \frac{dk_y}{T'} \left[ (V^2 e^{i(k_x \Omega + \phi_h)} + U^2 e^{i(k_x \Omega - \phi_h)}) a_{\mathbf{k}}^\dagger a_{\mathbf{k}} \right. \\ &\quad \left. + (U^2 e^{i(k_x \Omega + \phi_h)} + V^2 e^{i(k_x \Omega - \phi_h)}) b_{\mathbf{k}}^\dagger b_{\mathbf{k}} \right] + \mathbf{h.c.} \end{aligned} \quad (49)$$

This can also be expressed in matrix form as:

$$H_{NNN}(\mathbf{k}) = \int_0^T \frac{dk_x}{T} \int_0^{T'} \frac{dk_y}{T'} \psi_{\mathbf{k}}^\dagger \cdot h_{NNN}(\mathbf{k}) \cdot \psi_{\mathbf{k}} \quad (50)$$

$$\begin{aligned} h_{NNN}(\mathbf{k}) &= -2\eta V_{NNN} \begin{bmatrix} U^2 \cos(k_x \Omega + \phi_h) + V^2 \cos(k_x \Omega - \phi_h) & 0 \\ 0 & V^2 \cos(k_x \Omega + \phi_h) + U^2 \cos(k_x \Omega - \phi_h) \end{bmatrix} \\ \psi_{\mathbf{k}} &= \begin{bmatrix} b_{\mathbf{k}} \\ a_{\mathbf{k}} \end{bmatrix}. \end{aligned} \quad (51)$$

Importantly, we can rewrite  $h_{NNN}(\mathbf{k})$  as:

$$h_{NNN}(\mathbf{k}) = -2\eta V_{NNN} [\cos(k_x \Omega) \cos(\phi_h) \mathbb{I} + (U^2 - V^2) \sin(k_x \Omega) \sin(\phi_h) \sigma_z] \quad (52)$$

where we have used the normalization condition  $U^2 + V^2 = 1$ . This Hamiltonian, involving the linear combination of a component proportional to the identity matrix and a  $\mathbf{k}$ -dependent  $\sigma_z$  component, is as expected in the Haldane model. We further see that any phase  $\phi_h$  corresponding to a location in the topological phase diagram can be obtained experimentally, provided that  $U \neq V$ . By linearity, adding the contributions of  $h_{NN}(\mathbf{k})$  and  $h_{NNN}(\mathbf{k})$  in a regime where  $U^2 \gg V^2$  yields the desired, complete Haldane Hamiltonian.

## B. Derivation of the time-resolved transmission measured by the photodiode

The following derivation follows closely what is done in the supplementals of [34] without assuming perfect hybridization between the modes.

Assuming a CCW input field, the evolution of the electromagnetic field confined in the optical fibre loop cavity is given by the following Langevin equations:

$$\begin{aligned} \dot{d}_{m,\downarrow} &= i[H(t), d_{m,\downarrow}] - \frac{\gamma}{2} d_{m,\downarrow} \\ \dot{d}_{m,\uparrow} &= i[H(t), d_{m,\uparrow}] - \frac{\gamma}{2} d_{m,\uparrow} - i\sqrt{\kappa} s_{in}(t) \end{aligned} \quad (53)$$

where  $d_{m,\downarrow}$  and  $d_{m,\uparrow}$  are annihilation operators describing the CW and CCW modes respectively,  $H(t)$  is the sum of the EOM modulation and hybridization fibre coupler Hamiltonians,  $\kappa$  is the input-output coupling strength that quantifies the radiative loss rate,  $s_{in}$  is the input field given by  $s_{in} = F e^{-i\omega_L t}$ , and  $\gamma$  is the total decay rate of the field inside the cavity.

We then move to the coupled basis :

$$\begin{aligned} a_m &= U d_{m,\uparrow} + V d_{m,\downarrow} \\ b_m &= V d_{m,\uparrow} - U d_{m,\downarrow} \end{aligned} \quad (54)$$

where we pose  $U, V \in \mathbb{R}$  without loss of generality, the differential equations can be written in the rotating frame as:

$$\begin{aligned} \dot{\tilde{a}}_m &= i \left[ \tilde{H}(t), \tilde{a}_m \right] - \frac{\gamma}{2} \tilde{a}_m - iU\sqrt{\kappa} e^{i(m\Omega - \frac{\delta}{2})t} s_{in} \\ \dot{\tilde{b}}_m &= i \left[ \tilde{H}(t), \tilde{b}_m \right] - \frac{\gamma}{2} \tilde{b}_m - iV\sqrt{\kappa} e^{i(m\Omega + \frac{\delta}{2})t} s_{in} \end{aligned} \quad (55)$$

In Fourier space, this transforms into:

$$\begin{aligned} \dot{a}_{\mathbf{k}} &= i [H(\mathbf{k}), a_{\mathbf{k}}] - \frac{\gamma}{2} a_{\mathbf{k}} - iU\sqrt{\kappa} \sum_m e^{-i(k_x+k_y)m\Omega} e^{i(m\Omega - \frac{\delta}{2})t} s_{in} \\ \dot{b}_{\mathbf{k}} &= i [H(\mathbf{k}), b_{\mathbf{k}}] - \frac{\gamma}{2} b_{\mathbf{k}} - iV\sqrt{\kappa} \sum_m e^{-i(k_x+k_y)m\Omega} e^{i(m\Omega + \frac{\delta}{2})t} s_{in} \end{aligned} \quad (56)$$

We can then use the general basis that diagonalizes  $H(\mathbf{k})$ :

$$\begin{aligned} u_{\mathbf{k},+} &= \cos\left(\frac{\theta_{\mathbf{k}}}{2}\right) a_{\mathbf{k}} + \sin\left(\frac{\theta_{\mathbf{k}}}{2}\right) e^{i\phi_{\mathbf{k}}} b_{\mathbf{k}} \\ u_{\mathbf{k},-} &= \sin\left(\frac{\theta_{\mathbf{k}}}{2}\right) a_{\mathbf{k}} - \cos\left(\frac{\theta_{\mathbf{k}}}{2}\right) e^{i\phi_{\mathbf{k}}} b_{\mathbf{k}} \end{aligned} \quad (57)$$

with associated eigenenergies  $\omega_{\mathbf{k},\pm} = \epsilon_{\mathbf{k}}^{\pm}$  in which the equations of motion become:

$$\begin{aligned} \dot{u}_{\mathbf{k},+} &= -i\epsilon_{\mathbf{k}}^+ u_{\mathbf{k},+} - \frac{\gamma}{2} u_{\mathbf{k},+} - i\sqrt{\kappa} s_{in} \left[ U \cos\left(\frac{\theta_{\mathbf{k}}}{2}\right) e^{-i\frac{\delta}{2}t} + V \sin\left(\frac{\theta_{\mathbf{k}}}{2}\right) e^{i\frac{\delta}{2}t + i\phi(\mathbf{k})} \right] \sum_m e^{im\Omega(t-k_x-k_y)} \\ \dot{u}_{\mathbf{k},-} &= -i\epsilon_{\mathbf{k}}^- u_{\mathbf{k},-} - \frac{\gamma}{2} u_{\mathbf{k},-} - i\sqrt{\kappa} s_{in} \left[ U \sin\left(\frac{\theta_{\mathbf{k}}}{2}\right) e^{-i\frac{\delta}{2}t} - V \cos\left(\frac{\theta_{\mathbf{k}}}{2}\right) e^{i\frac{\delta}{2}t + i\phi(\mathbf{k})} \right] \sum_m e^{im\Omega(t-k_x-k_y)} \end{aligned} \quad (58)$$

Integrating over time, we obtain (assuming initial conditions  $u_{\mathbf{k},\pm}(0) = 0$ ):

$$\begin{aligned} u_{\mathbf{k},+}(t) &= -i\sqrt{\kappa} \int_0^t dt' e^{(i\epsilon_{\mathbf{k}}^+ + \gamma/2)(t'-t)} s_{in}(t') \left[ U \cos\left(\frac{\theta_{\mathbf{k}}}{2}\right) e^{-i\frac{\delta}{2}t'} + V \sin\left(\frac{\theta_{\mathbf{k}}}{2}\right) e^{i\frac{\delta}{2}t' + i\phi(\mathbf{k})} \right] \sum_m e^{im\Omega(t'-k_x-k_y)} \\ u_{\mathbf{k},-}(t) &= -i\sqrt{\kappa} \int_0^t dt' e^{(i\epsilon_{\mathbf{k}}^- + \gamma/2)(t'-t)} s_{in}(t') \left[ U \sin\left(\frac{\theta_{\mathbf{k}}}{2}\right) e^{-i\frac{\delta}{2}t'} - V \cos\left(\frac{\theta_{\mathbf{k}}}{2}\right) e^{i\frac{\delta}{2}t' + i\phi(\mathbf{k})} \right] \sum_m e^{im\Omega(t'-k_x-k_y)} \end{aligned} \quad (59)$$

Injecting the definition of  $s_{in}$  in these equations and doing the change of variable  $t'' = t - t'$ , they become:

$$\begin{aligned} u_{\mathbf{k},+} &= -i\sqrt{\kappa} \left[ U \cos\left(\frac{\theta_{\mathbf{k}}}{2}\right) C_1^+ + V \sin\left(\frac{\theta_{\mathbf{k}}}{2}\right) C_2^+ \right] \\ u_{\mathbf{k},-} &= -i\sqrt{\kappa} \left[ U \sin\left(\frac{\theta_{\mathbf{k}}}{2}\right) C_1^- - V \cos\left(\frac{\theta_{\mathbf{k}}}{2}\right) C_2^- \right] \end{aligned} \quad (60)$$

where we define

$$\begin{aligned} C_1^{(\pm)}(t) &= F e^{-i\omega_L t} e^{-i\frac{\delta}{2}t} \sum_m \left[ e^{im\Omega(t-k_x-k_y)} \int_0^t dt'' e^{-\frac{\gamma}{2}t''} e^{i(\omega_L - (m\Omega - \frac{\delta}{2} + \epsilon_{\mathbf{k}}^{\pm}))t''} \right] \\ C_2^{(\pm)}(t) &= F e^{-i\omega_L t} e^{i\frac{\delta}{2}t} e^{i\phi(\mathbf{k})} \sum_m \left[ e^{im\Omega(t-k_x-k_y)} \int_0^t dt'' e^{-\frac{\gamma}{2}t''} e^{i(\omega_L - (m\Omega + \frac{\delta}{2} + \epsilon_{\mathbf{k}}^{\pm}))t''} \right]. \end{aligned} \quad (61)$$

Under the assumption that the cavity's lifetime is much smaller than the time over which we integrate ( $\gamma^{-1} \ll t$ ) - which is reasonable as we wait 3  $\mu\text{s}$  before each experiment for the field to reach steady-state - these integrals are solved to :

$$\begin{aligned} C_1^{(\pm)}(t) &= -F e^{-i\omega_L t} e^{-i\frac{\delta}{2}t} \sum_m \left[ e^{im\Omega(t-k_x-k_y)} \frac{1}{i(\omega_L - (m\Omega - \frac{\delta}{2} + \epsilon_{\mathbf{k}}^{\pm})) - \frac{\gamma}{2}} \right] \\ C_2^{(\pm)}(t) &= -F e^{-i\omega_L t} e^{+i\frac{\delta}{2}t} e^{i\phi(\mathbf{k})} \sum_m \left[ e^{im\Omega(t-k_x-k_y)} \frac{1}{i(\omega_L - (m\Omega + \frac{\delta}{2} + \epsilon_{\mathbf{k}}^{\pm})) - \frac{\gamma}{2}} \right]. \end{aligned} \quad (62)$$

These functions therefore describe Lorentz distributions with evident resonance peaks happening at frequencies  $\omega_L = m\Omega - \frac{\delta}{2} + \epsilon_{\mathbf{k}}^{\pm}$  and  $\omega_L = m\Omega + \frac{\delta}{2} + \epsilon_{\mathbf{k}}^{\pm}$  with linewidth  $\frac{\gamma}{2}$ .

Let us now consider the transmitted field amplitude at the photodiode assuming detection of the CCW modes only:

$$\begin{aligned} s_{pd} &= s_{in} - i\sqrt{\kappa} \sum_m d_{m,\uparrow} \\ &= s_{in} - i\sqrt{\kappa} \sum_m \left[ U \tilde{a}_m e^{-i(m\Omega - \frac{\delta}{2})t} + V \tilde{b}_m e^{-i(m\Omega + \frac{\delta}{2})t} \right] \\ &= s_{in} - i\sqrt{\kappa} \sum_m \int_0^T \frac{dk_x}{T} \int_0^{T'} \frac{dk_y}{T'} \left[ U a_{\mathbf{k}} e^{-i(m\Omega - \frac{\delta}{2})t} e^{i(k_x+k_y)m\Omega} + V b_{\mathbf{k}} e^{-i(m\Omega + \frac{\delta}{2})t} e^{i(k_x+k_y)m\Omega} \right] \\ &= s_{in} - i\sqrt{\kappa} \sum_m \int_0^T \frac{dk_x}{T} \int_0^{T'} \frac{dk_y}{T'} \left[ U \left( \cos\left(\frac{\theta_{\mathbf{k}}}{2}\right) u_{\mathbf{k},+} + \sin\left(\frac{\theta_{\mathbf{k}}}{2}\right) u_{\mathbf{k},-} \right) e^{-i(m\Omega - \frac{\delta}{2})t} e^{i(k_x+k_y)m\Omega} \right] \\ &\quad - i\sqrt{\kappa} \sum_m \int_0^T \frac{dk_x}{T} \int_0^{T'} \frac{dk_y}{T'} \left[ V \left( \sin\left(\frac{\theta_{\mathbf{k}}}{2}\right) u_{\mathbf{k},+} - \cos\left(\frac{\theta_{\mathbf{k}}}{2}\right) u_{\mathbf{k},-} \right) e^{-i(m\Omega + \frac{\delta}{2})t} e^{i(k_x+k_y)m\Omega} \right]. \end{aligned} \quad (63)$$

This expression can be considerably simplified under the following approximations: first, we pose that the drive input field is resonant with the  $\bar{m}^{th}$  symmetric mode, i.e  $\omega_L \approx \bar{m}\Omega - \frac{\delta}{2}$ . Because we are in a regime where  $\gamma \ll \delta$ , this leads to only the  $C_1^{\pm}$  terms contributing significantly in  $u_{\mathbf{k},\pm}$ , letting us neglect  $C_2^{\pm}$  (which would correspond to a drive resonant with the  $\bar{m}^{th}$  anti-symmetric mode). Furthermore, every  $m \neq \bar{m}$  in the relations of the field amplitudes can be neglected. This gives rise to the simplified expressions :

$$\begin{aligned} u_{\mathbf{k},+}(t) &= -i \frac{\sqrt{\kappa} U \cos\left(\frac{\theta_{\mathbf{k}}}{2}\right) F e^{-i\omega_L t} e^{-i(k_x+k_y)\bar{m}\Omega} e^{i(\bar{m}\Omega - \frac{\delta}{2})t} e^{i\phi(\mathbf{k})}}{\gamma/2 - i(\Delta\omega_L - \epsilon_{\mathbf{k}}^+)} \\ u_{\mathbf{k},-}(t) &= -i \frac{\sqrt{\kappa} U \sin\left(\frac{\theta_{\mathbf{k}}}{2}\right) F e^{-i\omega_L t} e^{-i(k_x+k_y)\bar{m}\Omega} e^{i(\bar{m}\Omega - \frac{\delta}{2})t} e^{i\phi(\mathbf{k})}}{\gamma/2 - i(\Delta\omega_L - \epsilon_{\mathbf{k}}^-)}. \end{aligned} \quad (64)$$

where  $\Delta\omega_L = \omega_L - (\bar{m}\Omega - \frac{\delta}{2})$ . Second, we consider that the driving field is resonant with either the upper band or the lower band at a given time, but not with both. This is reasonable for most cases as we are usually in a regime where  $\gamma \ll |\epsilon_{\mathbf{k}}^{\pm}|$ ; thus, the condition  $|\Delta\omega_L - \epsilon_{\mathbf{k}}^{\pm}| \ll |\epsilon_{\mathbf{k}}^{\pm}|$  is only true for one band at a time. This enables us to neglect the contribution of the lower/upper band when considering the amplitude on the photodiodes of the upper/lower band independently. This approximation is however less accurate for  $\mathbf{k}$ -points where the linewidth is comparable to the size of the gap, and even less so at the positions of the Dirac points where  $\epsilon_{\mathbf{k}}^+ = \epsilon_{\mathbf{k}}^-$ . This causes small deviations in the value of the phases extracted at these points.

Under these two approximations, the expressions for the transmitted amplitude becomes:

$$\begin{aligned} s_{pd}^+ &= S_{in} - i\sqrt{\kappa} \sum_m \int_0^T \frac{dk_x}{T} \int_0^{T'} \frac{dk_y}{T'} e^{i(k_x+k_y)m\Omega} \left[ U \cos\left(\frac{\theta_{\mathbf{k}}}{2}\right) e^{-i(m\Omega - \frac{\delta}{2})t} e^{-i\phi_{\mathbf{k}}} + V \sin\left(\frac{\theta_{\mathbf{k}}}{2}\right) e^{-i(m\Omega + \frac{\delta}{2})t} \right] u_{\mathbf{k},+} \\ s_{pd}^- &= S_{in} - i\sqrt{\kappa} \sum_m \int_0^T \frac{dk_x}{T} \int_0^{T'} \frac{dk_y}{T'} e^{i(k_x+k_y)m\Omega} \left[ U \sin\left(\frac{\theta_{\mathbf{k}}}{2}\right) e^{-i(m\Omega - \frac{\delta}{2})t} e^{-i\phi_{\mathbf{k}}} - V \cos\left(\frac{\theta_{\mathbf{k}}}{2}\right) e^{-i(m\Omega + \frac{\delta}{2})t} \right] u_{\mathbf{k},-}. \end{aligned} \quad (65)$$

We now inject the simplified expressions for  $u_{\mathbf{k},\pm}$  in the above relations so that:

$$\begin{aligned} s_{pd}^+ &= F e^{-i\omega_L t} \left[ 1 - \kappa \sum_{m'} \int_0^T \frac{dk_x}{T} \int_0^{T'} \frac{dk_y}{T'} \frac{e^{im'\Omega(t-k_x-k_y)}}{\frac{\gamma}{2} - i(\Delta\omega_L - \epsilon_{\mathbf{k}}^+)} \left( U^2 \cos^2 \left( \frac{\theta_{\mathbf{k}}}{2} \right) + \frac{UV}{2} \sin(\theta_{\mathbf{k}}) e^{-i\delta t} e^{i\phi_{\mathbf{k}}} \right) \right] \\ s_{pd}^- &= F e^{-i\omega_L t} \left[ 1 - \kappa \sum_{m'} \int_0^T \frac{dk_x}{T} \int_0^{T'} \frac{dk_y}{T'} \frac{e^{im'\Omega(t-k_x-k_y)}}{\frac{\gamma}{2} - i(\Delta\omega_L - \epsilon_{\mathbf{k}}^-)} \left( U^2 \sin^2 \left( \frac{\theta_{\mathbf{k}}}{2} \right) - \frac{UV}{2} \sin(\theta_{\mathbf{k}}) e^{-i\delta t} e^{i\phi_{\mathbf{k}}} \right) \right] \end{aligned} \quad (66)$$

where we have defined  $m' = \bar{m} - m$ . Now, we note that  $\Omega \equiv \frac{2\pi}{T}$  by definition. Hence, we can use the identity

$$D_T(t-a) = \frac{1}{T} \sum_m e^{i(\frac{2\pi}{T})m(t-a)} \quad (67)$$

with  $D_T$  being a Dirac comb of period  $T$  that is defined as

$$D_T(t) = \sum_{n=-\infty}^{\infty} \delta(t-nT) \quad (68)$$

to further simplify the expressions for the transmitted amplitudes.

Integrating over  $\mathbf{k}$  is then very straightforward and yields:

$$\begin{aligned} s_{pd}^+ &= F e^{-i\omega_L t} \left[ 1 - \kappa \frac{U^2 \cos^2 \left( \frac{\theta_{\mathbf{k}}}{2} \right) + \frac{UV}{2} \sin(\theta_{\mathbf{k}}) e^{-i\delta t} e^{i\phi_{\mathbf{k}}}}{\frac{\gamma}{2} - i(\Delta\omega_L - \epsilon_{\mathbf{k}}^+)} \right]_{(k_x, k_y) = (t \bmod T, t \bmod T')} \\ s_{pd}^- &= F e^{-i\omega_L t} \left[ 1 - \kappa \frac{U^2 \sin^2 \left( \frac{\theta_{\mathbf{k}}}{2} \right) - \frac{UV}{2} \sin(\theta_{\mathbf{k}}) e^{-i\delta t} e^{i\phi_{\mathbf{k}}}}{\frac{\gamma}{2} - i(\Delta\omega_L - \epsilon_{\mathbf{k}}^-)} \right]_{(k_x, k_y) = (t \bmod T, t \bmod T')} \end{aligned} \quad (69)$$

The transmitted intensity measured by the photodiode is therefore given by:

$$\begin{aligned} I_{pd}^+ &= |s_{pd}^+|^2 \approx |F|^2 \left[ 1 - 2\kappa \operatorname{Re} \left\{ \frac{U^2 \cos^2 \left( \frac{\theta_{\mathbf{k}}}{2} \right) + \frac{UV}{2} \sin(\theta_{\mathbf{k}}) e^{-i\delta t} e^{i\phi_{\mathbf{k}}}}{\frac{\gamma}{2} - i(\Delta\omega_L - \epsilon_{\mathbf{k}}^+)} \right\} \right]_{(k_x, k_y) = (t \bmod T, t \bmod T')} + \mathcal{O} \left( \left( \frac{\kappa}{\gamma} \right)^2 \right) \\ I_{pd}^- &= |s_{pd}^-|^2 \approx |F|^2 \left[ 1 - 2\kappa \operatorname{Re} \left\{ \frac{U^2 \sin^2 \left( \frac{\theta_{\mathbf{k}}}{2} \right) - \frac{UV}{2} \sin(\theta_{\mathbf{k}}) e^{-i\delta t} e^{i\phi_{\mathbf{k}}}}{\frac{\gamma}{2} - i(\Delta\omega_L - \epsilon_{\mathbf{k}}^-)} \right\} \right]_{(k_x, k_y) = (t \bmod T, t \bmod T')} + \mathcal{O} \left( \left( \frac{\kappa}{\gamma} \right)^2 \right) \end{aligned} \quad (70)$$

where we neglect the quadratic term as we work in an under-coupling regime with  $\gamma > \kappa$ . We hence see that  $\mathbf{k}$  is related to the time variable via the relations introduced in Eq. 14, with the transmitted intensity exhibiting dips whenever the laser is resonant with an eigenmode and the time variable reaches the associated effective momentum.

### C. Anomalous transverse displacement and Chern number extraction

Our strategy to measure the photonic analogue of the transverse anomalous Hall current and then extract the Chern number of the topological bands is based on recent theoretical works [40, 41]. In these works, a link between the Berry curvature and the displacement of the light intensity profile under the effect of a synthetic electric field, i.e. a potential gradient in the photonic lattice, was put forward for driven-dissipative systems, generalizing to a non-equilibrium context well-known results of semi-classical electronic transport [28]. In particular, our experiment corresponds to the anomalous Hall regime of [40] where the linewidth of the photonic modes is much smaller than the overall width of the energy dispersion  $\epsilon_{\mathbf{k}}$  of the photonic band and smaller than the band gaps.

For lattices with equivalent sublattices, one has the relation

$$\delta r_x \simeq \frac{\int d^2\mathbf{k} \Omega(\mathbf{k}) n(\mathbf{k})^2 \gamma \lambda}{\int d^2\mathbf{k} n(\mathbf{k})} \frac{\gamma \lambda}{2} \simeq \frac{\bar{\Omega}(\omega_L) \lambda}{\gamma} \quad (71)$$

for a small force  $\lambda$  along the  $y$  direction. Here,  $\delta \mathbf{r}$  is the spatial shift of the center-of-mass of the intensity distribution

$$\delta \mathbf{r} = \frac{\sum_{\mathbf{r}} \mathbf{r} I_{\mathbf{r}}^{(\lambda)}}{\sum_{\mathbf{r}} I_{\mathbf{r}}^{(\lambda)}} - \frac{\sum_{\mathbf{r}} \mathbf{r} I_{\mathbf{r}}^{(\lambda=0)}}{\sum_{\mathbf{r}} I_{\mathbf{r}}^{(\lambda=0)}} \quad (72)$$



Note that in this formula, the position  $\mathbf{r}$  runs over the unit cells and, for each value of the applied force  $\lambda$ ,  $I_{\mathbf{r}}^{\lambda} = \sum_l I_{\mathbf{r},l}^{\lambda}$  is the total intensity in the unit cell, obtained by summing over the sub-sites  $l$  as if these were located at the same position  $\mathbf{r}$ . Then,  $n(\mathbf{k}) = [(\epsilon_{\mathbf{k}} - \omega_L)^2 + (\gamma/2)^2]^{-1}$  is the population of the different  $\mathbf{k}$ -space modes and  $\Omega(\omega_L)$  is the average value of the Berry curvature over all resonant modes  $\epsilon_{\mathbf{k}} = \omega_L$ . The coherent drive at frequency  $\omega_L$  is assumed to drive a single sub-site of the unit cell. For the assumed small value of the linewidth  $\gamma$  of the photonic modes, only a single band is effectively excited by the drive and the other bands are far enough in energy to be neglected.

If the photonic lattice has two non-equivalent sites per unit cell, a slightly more sophisticated approach must be used, first derived in [41]. An averaged displacement is defined here as

$$\delta \mathbf{r} = \frac{\sum_m \sum_{\mathbf{r}} \mathbf{r} I_{\mathbf{r}}^{(m,\lambda)}}{\sum_m \sum_l I_{\mathbf{r}}^{(m,\lambda)}} - \frac{\mathbf{r} I_{\mathbf{r}}^{(m,\lambda=0)}}{\sum_m \sum_l I_{\mathbf{r}}^{(m,\lambda=0)}} \quad (73)$$

where  $I_{\mathbf{r}}^{(m,\lambda)}$  refers again to the total intensity within a unit cell and the index  $m$  corresponds to the specific (single) sub-site on which the drive is located.

This quantity is then related to the Berry curvature by the generalized formula

$$\delta r_i = \frac{1}{\int d^2 \mathbf{k} n(\mathbf{k})} \sum_j \left\{ - \int d^2 \mathbf{k} n(\mathbf{k})^2 \Omega_{ij}(\mathbf{k}) + \int d^2 \mathbf{k} (\omega_L - \epsilon_{\mathbf{k}}) [2n(\mathbf{k})^2 g_{ij}(\mathbf{k}) + 2n(\mathbf{k})^3 \partial_i \epsilon_{\mathbf{k}} \partial_j \epsilon_{\mathbf{k}}] \right\} \frac{\gamma E_j}{2} \quad (74)$$

where  $i, j = \{x, y\}$  run over the Cartesian directions,  $\Omega_{ij} = \varepsilon_{ij} \Omega(\mathbf{k})$  is the (antisymmetric) Berry curvature tensor,  $g_{ij}$  is the (symmetric) quantum metric tensor.

What is relevant in our experiment is the response  $\delta r_x$  under the force  $E_y$ . In the absence of any staggered on-site potential  $\Delta = 0$ , the second term of the integrand involving the quantum metric  $g_{xy}(\mathbf{k})$  and the derivatives of the dispersion relation  $\partial_x \omega(\mathbf{k})$  integrates to zero because both of these terms are odd in  $k_x$ ,  $g_{xy}(-k_x, k_y) = -g_{xy}(k_x, k_y)$  and  $\partial_{k_x} \epsilon_{-k_x, k_y} = -\partial_{k_x} \epsilon_{k_x, k_y}$ . Thus, for the extraction of the Chern number, we can restrict to the first term in the integrand, which involves the Berry curvature. In this  $\Delta = 0$ , the contributions of the different sub-lattices  $m$  to (73) are equal, which allows to only evaluate the quantities for a single  $m$ .

In the general case of an arbitrary  $\Delta$ , one could still extract the term involving the Berry curvature  $\Omega$  by repeating the measurement with forces along  $x$  or  $y$  and then taking the difference to isolate the (antisymmetric) Berry contribution from the (symmetric) ones involving the quantum metric and the group velocity [41]. This would provide information on the distribution of the Berry curvature across the BZ.

The main goal of our work is the experimental measurement of the Chern number. To this purpose, one has to integrate the Berry curvature across the Brillouin zone. This can be performed by repeating the measurement of the transverse displacement for different values of the driving laser frequency and summing up the results. It is interesting to note that, upon such an integral, the terms in (74) proportional to  $\omega_L - \epsilon_{\mathbf{k}}$  automatically vanish as they are odd in this quantity ( $n(\mathbf{k})$  is instead even) and one is naturally left with the Berry curvature term only.

In practice, we call  $\delta x_{\omega_L}$  the displacement experimentally measured for a coherent drive at  $\omega_L$  and a force along  $y$  of strength  $\lambda$ , and correspondingly  $n(\mathbf{k}, \omega_L)$  the resonant population of the mode at  $\mathbf{k}$ . From (74), we then have

$$\delta x_{\omega_L} \int d^2 \mathbf{k} n(\mathbf{k}, \omega_L) = -\frac{\lambda \gamma}{2} \int d^2 \mathbf{k} \Omega(\mathbf{k}) n(\mathbf{k}, \omega_0)^2. \quad (75)$$

Integrating both sides over  $\omega_L$  within the band of interest, we obtain

$$\begin{aligned} \int_{\text{band}} d\omega_L \delta x_{\omega_L} \int d^2 \mathbf{k} n(\mathbf{k}, \omega_L) &= -\frac{\lambda \gamma}{2} \int_{\text{band}} d\omega_L \int d^2 \mathbf{k} \Omega(\mathbf{k}) n(\mathbf{k}, \omega_L)^2 = \\ &= -\frac{\lambda \gamma}{2} \int d^2 \mathbf{k} \Omega(\mathbf{k}) \int_{\text{band}} d\omega_L n(\mathbf{k}, \omega_L)^2 = -\frac{\lambda \gamma}{2} \int d^2 \mathbf{k} \Omega(\mathbf{k}) \frac{4\pi}{\gamma^3} = -\frac{4\pi^2 \lambda}{\gamma^2} \mathcal{C} \end{aligned} \quad (76)$$

where on the right-hand side we have exchanged the order of the integrals and, then, analytically performed the one of the squared resonant function over  $\omega_L$ : the remaining integral over  $\mathbf{k}$  is the definition of Chern number  $\mathcal{C}$ .

This formula provides a straightforward way to extract the Chern number from a suitable average of the experimentally observed displacement  $\delta x_{\omega_0}$  weighted by a factor  $n(\mathbf{k}, \omega_L) = [(\epsilon_{\mathbf{k}} - \omega_L)^2 + (\gamma/2)^2]^{-1}$  which is also experimentally extracted from the measured band dispersion,

$$\mathcal{C} = -\frac{\gamma^2}{4\pi^2 \lambda} \int_{\text{band}} d\omega_L \delta x_{\omega_L} \int d^2 \mathbf{k} n(\mathbf{k}, \omega_L). \quad (77)$$

The values of the Chern number indicated in Fig. 4 of the main text are obtained using this procedure.